Nanoscale Advances

ROYAL SOCIETY OF CHEMISTRY

PAPER

View Article Online
View Journal | View Issue

Cite this: *Nanoscale Adv.*, 2025, **7**, 6828

A nano-powered green and chemically synthesized Au/MWCNT modified electrochemical sensor for methylene blue detection in river water

Seleke J. Mokole[ab] and Omolola E. Fayemi *[ab]

This study explores the development of novel gold nanoparticle (AuNP) and multi-walled carbon nanotube (MWCNT) nanocomposites for methylene blue (MB) dye detection, leveraging both green (Au_{grn}) and chemical (Au_{chm}) synthesis methods. A thorough analysis of the nanomaterials synthesized using green and chemical routes was performed utilizing Fourier transform infrared (FTIR) spectroscopy, scanning electron microscopy (SEM), and transmission electron microscopy (TEM), revealing particle sizes of 13.66 nm and 14.86 nm for Au_{chm} and Au_{grn}, respectively. UV-visible spectroscopy (UV) and X-ray diffraction (XRD) reveal crystallite sizes ranging from 5.36 nm to 21.26 nm. Electrochemical analysis *via* cyclic voltammetry (CV), electrochemical impedance spectroscopy (EIS), and square-wave voltammetry (SWV) revealed distinct current responses among the synthesized materials. EASA, which is the electrochemical active surface area of the electrodes was calculated, and the values were 0.053 cm^2 (Au_{chm}/MWCNTs), 0.031 cm^2 (Au_{grn}/MWCNTs), 0.024 cm^2 (MWCNTs), 0.006 cm^2 (Au_{grn}), 0.005 cm^2 (Au_{chm}), and 0.002 cm^2 (bare). EIS showed R_{ct} values in the following order: 32.20 Ω < 34.02 Ω < 36.61 Ω < 3.4 × 10^5 Ω < 3.7 × 10^5 Ω < 5.6 × 10^5 Ω for Au_{grn}/MWCNTs, MWCNTs, Au_{chm}/MWCNTs, Au_{chm}, Au_{grn}, and bare electrode, respectively, which correlated with CV oxidation peaks in FeCN, except for the bare electrode due to the *n*-value of 0.87. The oxidation current response in MB decreased in the order of 124.29 μA for MWCNTs, 114.77 μA for Au_{grn}/MWCNTs, 60.85 μA for Au_{chm}/MWCNTs, 18.96 μA for Au_{chm}, 2.81 μA for bare, and 2.08 μA for Au_{grn}. The limits of detection (LOD) and quantification (LOQ) were determined to be 20.62 nM and 62.51 nM for Au_{chm}/MWCNTs and 20.23 nM and 61.30 nM for Au_{grn}/MWCNTs, respectively, indicating slightly superior sensitivity for Au_{grn}/MWCNTs. Analysis of real-life environmental samples demonstrated the practical applicability of the synthesized electrodes, with recovery percentages ranging from 90% to 107% (n = 3). These findings underscore the dependability and sensitivity of the developed nanocomposites for MB detection.

Received 23rd April 2025
Accepted 20th July 2025

DOI: 10.1039/d5na00396b

rsc.li/nanoscale-advances

1 Introduction

Water pollution is a world challenge. Globally, water pollution is a significant contributor to illness and death, with approximately 80% of diseases and half of all child fatalities attributed to contaminated water.[1] The second largest water-polluting industry is the textile industry, which contributes about 17–20% and 8% towards carbon emissions.[2] The textile industry's excessive water usage leads to water scarcity, and its wastewater discharge causes severe environmental degradation, affecting agriculture, water sources, grasslands, and aquatic ecosystems. Moreover, the absence of practical solutions to mitigate the sector's environmental impacts, including resource depletion, greenhouse gas emissions, and the release of hazardous materials, exacerbates environmental and human health risks.[3] One of the dyes produced and used by the textile industry is methylene blue (MB) dye, MB is a synthetic dye widely used in various industries, including textiles, the food industry (as a food additive), cosmetics, and pharmaceuticals. While MB has some medicinal benefits when used safely and as prescribed, its release into the environment through untreated wastewater poses significant health risks. Human exposure to MB can lead to serious health problems, such as cyanosis, tissue damage, and nausea. Additionally, MB can harm plants, inhibit growth, and reduce pigment and protein content. The environmental impact of MB pollution is alarming, contributing to water scarcity and the need for effective removal methods before industrial discharge.[4–13] MB is a complex molecule that is resistant to degradation due to its stability against light, temperature, and chemicals. Its hydrophilic nature and

[a]*Department of Chemistry, School of Physical and Chemical Sciences, Faculty of Natural and Agricultural Sciences, North-West University (Mafikeng Campus), Private Bag X2046, Mmabatho, 2735, South Africa. E-mail: Omolola.Fayemi@nwu.ac.za*

[b]*Material Science Innovation and Modelling (MaSIM) Research Focus Area, Faculty of Natural and Agricultural Sciences, North-West University (Mafikeng Campus), Private Bag X2046, Mmabatho, 2735, South Africa*

persistence in water contribute to significant environmental pollution.[14]

Since high concentration levels of MB dye has always been a great concern to both human health and the environment, various analytical methods were previously employed for its detection such as spectrophotometry (UV-vis spec),[15] capillary electrophoresis (CE),[16] cation exchange chromatography coupled to electrospray ionisation tandem mass spectroscopy (CEC-ESI-MS/MA),[17] liquid chromatography (LC),[18,19] and liquid chromatography-tandem mass spectroscopy (LC-MS/MS).[20] Even though these methods have done exceptional work for the determination of MB, they also have several disadvantages, which include extensive labour requirements in sample preparation, requiring highly trained personnel for implementation, low sensitivity as a result of their complexity level, and long processing time.[21] Electrochemical sensors are some of the devices used to detect MB dye. Several challenges impede the efficacy of sensors, including sensitivity and selectivity issues, wherein the differentiation between target analytes and interfering substances proves difficult, thereby compromising sensitivity.[22,23] Since electrochemical sensors are used for detecting various analytes, such as metronidazole (MTZ), which is an antibiotic, the electrodes used play a crucial role in determining their effectiveness. For instance, the nitro group ($-NO_2$) in MTZ is readily reduced at bare electrodes like gold, glassy carbon, and carbon paste electrodes. However, these bare electrodes are prone to MTZ adsorption, leading to surface contamination by reducible species, which compromises the feasibility, sensitivity, detection limit, repeatability, and selectivity of the redox reactions. To address these issues, modified electrodes incorporating metal oxides, nanoparticles, nanocomposites, conducting polymers, or redox mediators have been employed, showcasing improved electrocatalytic properties, larger surface areas, reduced interference, and enhanced sensitivity, reproducibility, and selectivity. This highlights the need for surface modification to achieve reliable and accurate detection of analytes like metronidazole, similar to the challenges observed with dye in water.[24,25] Moreover, the accuracy and reproducibility of these sensors can be further compromised by non-specific adsorption of interfering species, complex sample matrices, and variability in nanomaterial synthesis, which can lead to inconsistent sensor performance across different batches.[22,23,26]

Electrochemical sensors are advanced tools that convert chemical reactions or the presence of specific molecules into a measurable electrical response, enabling the detection and quantification of target species.[27] The convergence of nanoscience and nanotechnology has transformed the landscape of electrochemical sensors, enabling the creation of nanomaterials that dramatically enhance their performance. Leveraging the distinct properties of nanomaterials, such as exceptional conductivity and expansive surface areas, has yielded numerous advantages, including bolstered stability, streamlined electron transfer, augmented catalytic capabilities, intensified signal output, efficient biomolecule immobilization, and remarkably improved selectivity and sensitivity.[28–33] To overcome sensor-related challenges, electrochemical sensors employ a multifaceted approach to overcome challenges related to sensitivity, selectivity, non-specific adsorption, and matrix effects. To enhance sensitivity and selectivity, advanced materials like MWCNTs and graphene are utilized to modify electrodes, improving the electrocatalytic activity and reducing interference. Surface functionalization with specific polymers or ligands prevents non-specific adsorption, while multi-electrode systems with varied modifications enable better discrimination of target analyte signals against background noise.[34–37] Furthermore, advanced signal processing techniques, including machine learning and methods like Square Wave Voltammetry (SWV) and differential pulse voltammetry, are employed to analyze complex data patterns and improve the detection accuracy. The use of three-electrode systems and *in situ* regeneration of the sensor surface also contribute to minimizing interference and maintaining sensitivity over time. By integrating these strategies, electrochemical sensors can achieve high sensitivity, selectivity, and accuracy, even in complex matrices.[26,33,36–41]

Bare electrodes often exhibit limited electrochemical activity, sensitivity, stability, and reproducibility compared to modified electrodes. To enhance the sensing performance, modifications with metal oxides (such as Fe, W, and Ti oxides), metal nanoparticles (Ag, Au, and Cu), and carbon-based materials like MWCNTs and graphene have been explored.[42] MWCNTs offer a large surface area, high conductivity, and abundant active sites, making them suitable for electrochemical sensing applications. When combined with metal nanoparticles or metal oxides, these nanocomposites can exhibit improved electrocatalytic properties, stability, and sensitivity, enabling more accurate detection of analytes. MWCNTs exhibit outstanding properties that render them exceptionally suitable for electrochemical sensors, particularly in the detection of MB.[43,44] Their unique combination of high electronic conductivity, extensive surface area, and robust chemical stability synergistically enhances sensitivity and selectivity, enabling detection limits as low as 0.21 nM for MB. Functionalization of MWCNTs with amino groups significantly increases electrocatalytic activity, while their large surface area facilitates increased interaction with MB molecules.[36,43,44] Furthermore, MWCNTs demonstrate remarkable regeneration potential, allowing for repeated use after treatment, and exhibit cost-effectiveness due to their relatively low production costs compared to single-walled carbon nanotubes. The adsorption of MB onto MWCNTs is mainly governed by electrostatic attraction between the positively charged MB molecules and the negatively charged functional groups on the MWCNT surface, leading to improved adsorption efficiency and kinetic rate. Supplementing these interactions are mechanisms such as π–π stacking and hydrogen bonding, which collectively contribute to the outstanding performance of MWCNTs in capturing MB from aqueous solutions, underscoring their potential for environmental monitoring and industrial applications.[44–46]

Chemically synthesized gold nanoparticles (AuNPs) exhibit several advantageous properties for electrochemical sensors,

particularly in detecting MB dye. These properties include high electrocatalytic activity, stability, and uniformity, which enable improved sensitivity and response time.[47,48] The high surface-to-volume ratio of chemically synthesized AuNPs provides increased binding sites for target analytes, enhancing detection capabilities.[48,49] Furthermore, the physicochemical properties of these AuNPs can be adjusted by varying synthesis conditions, allowing for optimization in sensor applications. This control over size and shape leads to more stable and uniform nanoparticles that reduce aggregation and maintain high reactivity.[47–49] In contrast, green synthesized AuNPs offer distinct benefits, including eco-friendliness, cost-effectiveness, simplicity, and scalability.[50–53] This method utilizes non-toxic, biodegradable materials, reducing the environmental impact and lowering production costs. Green synthesized AuNPs also exhibit enhanced biocompatibility, making them suitable for biomedical applications. Moreover, the electron transfer rate of green synthesized AuNPs is significantly enhanced, facilitating rapid electron transfer between the electrode and analyte. This improvement is attributed to increased conductivity, electrocatalytic activity, and lower charge transfer resistance.[50–55]

Regardless of the synthesis method, AuNPs possess unique properties that make them ideal for electrochemical sensors. Their high surface-to-volume ratio contributes to increased reactivity, sensitivity, and optimal functionalization.[55–59] The localized surface plasmon resonance (LSPR) effect, resulting from this ratio, enables efficient signal transduction mechanisms. Additionally, AuNPs exhibit excellent electrocatalytic activity, improving sensitivity in detecting analytes like MB, with limits of detection as low as 2.935 pM, as reported earlier. They also facilitate faster electron transfer, leading to increased reaction rates for redox processes, and amplify the current response in electrochemical measurements. Overall, the integration of AuNPs in electrochemical sensors offers a promising approach for enhancing the sensitivity, selectivity, and stability in various applications.[50–60]

The integration of AuNPs and MWCNTs in electrochemical sensors yields composites with enhanced electrocatalytic performance, electron transfer capabilities, and stability.[61–63] The synergistic effect of AuNPs decorating MWCNTs increases the electroactive surface area, leading to improved electron transfer rates and overall sensor sensitivity. This combination also promotes covalent bonding between AuNPs and MWCNTs, strengthening the composite structure and reducing the likelihood of MWCNT aggregation and degradation. The binding between AuNPs and MWCNTs is facilitated through multiple mechanisms, including covalent bonding *via* thiol groups, electrostatic interactions between charged functional groups, and π–π stacking interactions between the aromatic structures of MWCNTs and the surface of AuNPs. These mechanisms collectively create a robust interface between AuNPs and MWCNTs, enhancing their performance in electrochemical sensors. The resulting AuNP/MWCNT composites exhibit improved sensitivity, mechanical strength, and electrochemical properties, making them suitable for various sensing applications.[64–66] The increased surface area and electroactive sites enable better detection of analytes, while the stability and adaptability of the composites ensure consistent performance in complex environments.[62,63,67]

This research paper offers a novel contribution to the field of nanotechnology and environmental sensing by providing a comprehensive comparison of the properties and performance of Au/MWCNT nanocomposites synthesized *via* chemical and green routes. The study's focus is on synthesizing Au/MWCNTs using green and chemical synthesis routes, characterizing the nanomaterials by UV-vis spec, FTIR, XRD, SEM, and TEM analyses, and determining their electrochemical properties using CV, EIS, and SWV. Green and chemically synthesis routes for Au/MWCNTs are compared, and their electrochemical properties in river water for monitoring MB dye are compared. Using these nanocomposites addresses a critical environmental issue, while the benchmarking of the sensors against existing literature provides a nuanced understanding of their potential for real-life applications. Moreover, the investigation of green synthesis routes as a viable alternative to traditional chemical methods adds a new dimension to the field, highlighting the possibility of developing environmentally friendly sensing materials that can mitigate the impact of toxic dyes on aquatic ecosystems.

2 Methods and materials

2.1 Chemicals

Sodium phosphate monobasic NaH_2PO_4 (99%) and sodium phosphate dibasic Na_2HPO_4 (99%), purchased from LABCHEM and GlassWorld located in Johannesburg, South Africa for the preparation of phosphate buffer solution, gold(III) chloride trihydrate (99.9%) ($HAuCl_4 \cdot 3H_2O$), aluminium oxide (Al_2O_3), sodium hydroxide (NaOH) (98%), potassium hexacyanoferrate(III) ($K_3[Fe(CN)_6]$) (99%) and potassium hexacyanoferrate(IV) (K_4[Fe(CN)6]) (99%) for ferrocyanide solution, hydrochloric acid (HCl) (32%), trisodium citrate dihydrate ($Na_2C_6H_5O_7 \cdot 2H_2O$), methylene blue dye ($C_{16}H_{18}ClN_3S$) (analytical-grade form), *N*,*N*-dimethylformamide (C_3H7NO) (USA) (99%), nitric acid (32%) (HNO_3), potassium chloride (99%) (KCl), sodium borohydride ($NaBH_4$) (95%), and multi-walled carbon nanotubes (MWCNTs) obtained from Merck Pty Ltd (Darmstadt, Germany).

2.2 Equipment

Characterization and analysis were carried out using various equipment, including an X-ray diffractometer (Bruker D8, Karlsruhe, Germany) for examining the crystalline structure over a 2θ Bragg's range of 0–90°. A Quanta FEG-250 field emission gun scanning electron microscope (Thermo Fisher Scientific, USA) was used for structural characterization. Fourier transform infrared spectroscopy was performed using an Opus Alpha-P FT-IR spectrometer (Bruker Optics Incorporation, USA) within the 4000–500 cm^{-1} wavenumber range. UV-vis analysis was conducted using a Spectroquant Prove 600 spectrophotometer (Merck KGaA, Germany) over the 200–800 nm range. Electrochemical studies were facilitated by an AUTOLAB PGSTAT302N potentiostat–galvanostat (Eco Chemie,

Netherlands) with NOVA software, utilizing a three-electrode system consisting of a platinum counter electrode, a glassy carbon working electrode, and a Ag/AgCl reference electrode with 3 M KCl (Metrohm, South Africa)

2.3 Gold nanoparticle chemical synthesis

0.1 g of $HAuCl_4 \cdot 3H_2O$ and 0.1 g of $Na_2C_6H_5O_7$ were dissolved in 10 ml of water separately creating a 1% w/v solution for each chemical. The $HAuCl_4 \cdot 3H_2O$ solution was stirred vigorously while slowly adding drops of $NaBH_4$ (0.05 g), which was prepared in 5 ml of ice-cold distilled water until the gold solution turned pale yellow. After the solution turned pale yellow, sodium citrate solution was added, and the mixture was continued stirring for 30 min. The resulting mixture was placed in a centrifuge for 10 min at 10 000 rpm. The supernatant was washed with distilled water and dried at 60 °C in an oven to obtain a gold nanoparticle powder.[68]

2.4 Gold nanoparticle green synthesis

A straightforward green synthesis method was employed to fabricate silver nanoparticles (AuNPs) using the *Hypoxis hemerocallidae corm* plant extract. The process began with boiling 5 g of powdered leaves in 250 ml of distilled water for 10 min, followed by filtration and storage. Next, 40 ml of the plant extract was combined with a 0.001 M silver nitrate solution at room temperature and was allowed to react overnight, facilitating the formation of nanoparticles. Finally, the resulting AuNPs were centrifuged at 1000 rpm for 15 min to yield purified nanoparticles and were dried at 70 °C for 8 hours.[69]

2.5 Nanocomposite formation

For each synthesis route, three different ratios (1 : 1, 1 : 2, and 1 : 3) of MWCNTs : Au nanoparticles were prepared. The proportion of Au nanoparticles was varied, while that of MWCNTs was kept constant. MWCNTs and Au nanoparticles were mixed in a vial, and 3 ml of DMF was added. The mixtures of different ratios were stirred for 48 h. The resulting paste was used in electrode optimization studies, and the ratio with the highest current response was used for further electrochemical studies for each synthesis route.[70]

2.6 Electrode pre-treatment process

To clean and activate the electrode, a mixture of 5 g Al_2O_3 and 3 ml distilled water was prepared on the three-electrode cleaning cloths of different textures. Infinity patterns were traced on the surface of the electrode using an electrode cleaning material, followed by immersion in a beaker of 35 ml distilled water, placing in a sonicator for 5 min, then placing in a beaker containing 35 ml of ethanol for 5 min, and again in the beaker of 35 ml distilled water for 5 min to remove all residues and impurities. The clean and activated electrode was placed in an oven for 5 min at 50 °C. To modify the electrode after drying, 0.1 ml of Au/MWCNTs was drop-cast onto the 3 mm surface of the glassy carbon electrode (GCE) using a Pasteur pipette, and it was dried in an oven at 50 °C for 5 to 7 min.[70]

2.7 Optimal pH determination

The optimization of electrolyte and pH conditions was crucial for enhancing the electrochemical performance of Au_{chm}/MWCNT and Au_{grn}/MWCNT electrodes. Initially, various electrolytes (HCl, H_2SO_4, PBS, KCl, and NaCl) were screened at pH 4, and HCl emerged as the optimal choice due to its superior oxidation and reduction peaks for MB. Subsequently, a pH optimization study was conducted using NaCl as the electrolyte, with pH values ranging from 3.0 to 9.0. pH 5.0 yielded the highest current response for both Au_{chm}/MWCNT and Au_{grn}/MWCNT electrodes. pH adjustments were made using NaOH and HNO_3. Therefore, pH 5.0 was used for further experiments.

2.8 Concentration studies

To evaluate the selectivity, limit of detection (LOD), and limit of quantification (LOQ) of the Au/MWCNT nanocomposites, square wave voltammetry (SWV) was employed using an Autolab setup. The SWV parameters were optimized as follows: a potential range of 0.0–1.0 V, potential amplitude of 0.01 V, frequency of 10 Hz, and potential step of 0.01 V. Using this optimized setup, the electrode was utilized to measure the response of the Au/MWCNT nanocomposites to varying concentrations of MB, ranging from 19.08 to 102.05 nM. This allowed for the assessment of the sensitivity of the nanocomposites towards MB.

2.9 Interference studies

For the investigation of selectivity and electrochemical response of the Au/MWCNT nanocomposites synthesized *via* both green and chemical methods, SWV was employed over a potential range of −0.4 to 1.2. The SWV parameters were set as follows: an amplitude of 0.01 V, a frequency of 10 Hz, and a step potential of 0.01 V. Using this optimized setup, the electrode was utilized to measure the response of the Au/MWCNT nanocomposites to varying concentrations of MO and SSY, ranging from 0.95 to 5.10 μM. This enabled the evaluation of the selectivity of both green and chemically synthesized nanocomposites towards these target analytes.

2.10 Analysis of real-life environmental samples

5 ml of river water sample was mixed with HCl solution (5 ml) (pH 5.0) and agitated for 10 min to create a homogeneous mixture. Subsequently, varying concentrations of MB were added to the mixture to simulate spiked samples. The resulting solutions, including the un-spiked control, were then analyzed using both chemically and green synthesized Au/MWCNT nanocomposites to quantify the MB concentrations.

3 Discussion of results

3.1 UV-vis spectral analysis

Fig. 1 presents the UV-vis spectra of all the nanocomposites and their pristine nanoparticles. Fig. 1(a) shows a peak at 513.17 and Fig. 1(b) shows a peak at 539.22 nm for Au_{chm} and Au_{grn}, respectively, with the peak of Au_{chm} being narrower than that of

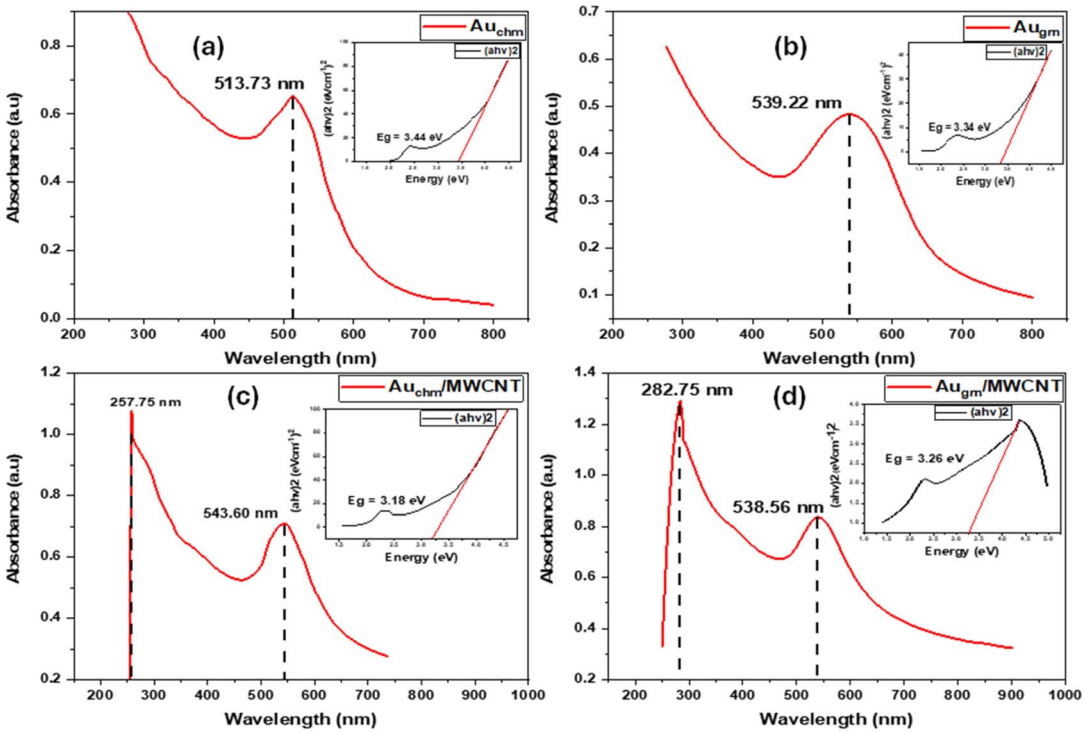

Fig. 1 The optical absorption spectra of (a) Au_{chm}, (b) Au_{grn}, (c) Au_{chm}/MWCNTs, and (d) Au_{grn}/MWCNTs. The inserted images are the Tauc plots for each nanomaterial.

Au_{grn}, indicating the smaller particle size of chemically synthesized AuNPs. The peaks at 513.73 and 539.22 nm are attributed to surface plasmon excitation, a Au nanoparticle characteristic.[71–73] In Fig. 1(c) and (d), the spectra of the nanocomposites show the presence of peaks for AuNPs in the range of 500–600 nm and for MWCNTs in the range from 200 to 300 nm;[70] the peak at 254.24 nm in both spectra shows the efficient functionalization of MWCNTs because it is due to the π transition of the antibonding COOH group, and the peak at 276.02 nm is attributed to the π–π* transition of the sp^2-hybridized C=C aromatic carbons in MWCNTs,[70,74,75] indicating the correct and proper decoration of AuNPs on the surface of MWCNTs. However, the Au_{chm}/MWCNT nanocomposite shows a red shift in surface plasmon resonance (SPR), indicating an increase in refractive index around AuNPs, suggesting a stronger interaction between AuNPs and MWCNTs, attributed to the covalent bonds between AuNPs and the walls of MWCNTs. This interaction leads to a change in the local refractive index around the AuNPs, causing a shift in the SPR band to longer wavelengths. Similar observations have been reported in the literature, where the attachment of AuNPs to MWCNTs results in a red shift due to the strong interaction between the two materials.[76] The Au_{grn}/MWCNTs showed a blue shift in SPR, indicating a decrease in the refractive index around AuNPs due to less interaction between AuNPs and MWCNTs, which also shows a reduction in particle size.[77–81] According to the literature, the decrease in the dielectric constant near the AuNP surface can cause a blue shift in the SPP peak. This decrease can occur when biomolecules are desorbed from the AuNP surface (as observed in the case of citrate ions[82]), such as upon interaction with MWCNTs. The resulting change in the dielectric environment affects the electron cloud's oscillation frequency, leading to a blue shift, consistent with the observed UV spectra.[83] By extrapolating the linear portion of $(\alpha h\nu^2)$ *vs.* $(h\nu)$, the band gap energy was found to be 3.44, 3.54, 4.57, 3.18, and 3.26 eV for Au_{chm}, Au_{grn}, MWCNTs, Au_{chm}/MWCNTs, and Au_{grn}/MWCNTs, respectively. Both nanocomposites showed a lower bandgap energy than their pristine nanoparticles, indicating that they are more effective in catalysis, better conductivity and electric properties as they can absorb a broader spectrum of light and improve the charge carrier mobility as less energy is required to excite charge carriers.[84]

3.2 FTIR analysis

FTIR spectra of Au/MWCNT nanocomposites and pristine nanoparticles were recorded in the 4000 to 500 cm^{-1} range. Fig. 2(a) shows peaks at 588.04 cm^{-1}, attributed to the Au–O vibration, and 940.82 cm^{-1}, attributed to the C–O and C–C stretching vibrations from citrate molecules adsorbed on the AuNP surface. Peaks at 1234.93 and 1633.59 cm^{-1} represent $-COO^-$ symmetric and asymmetric stretching vibrations, indicating the presence of carboxylate groups. The peak at 2130.04 cm^{-1} indicates the presence of cyanide (Au–CN) stretching vibration, coming from the decomposition of $NaBH_4$ and also its reaction with $HAuCl_4$ influencing the stability of AuNPs, and the peak at 3265.85 cm^{-1} shows the presence of the hydroxyl group of the citrate molecule.[85–87] Fig. 2(b) shows peaks at 568.49 cm^{-1} indicating the binding of AuNPs to oxygen-containing functional

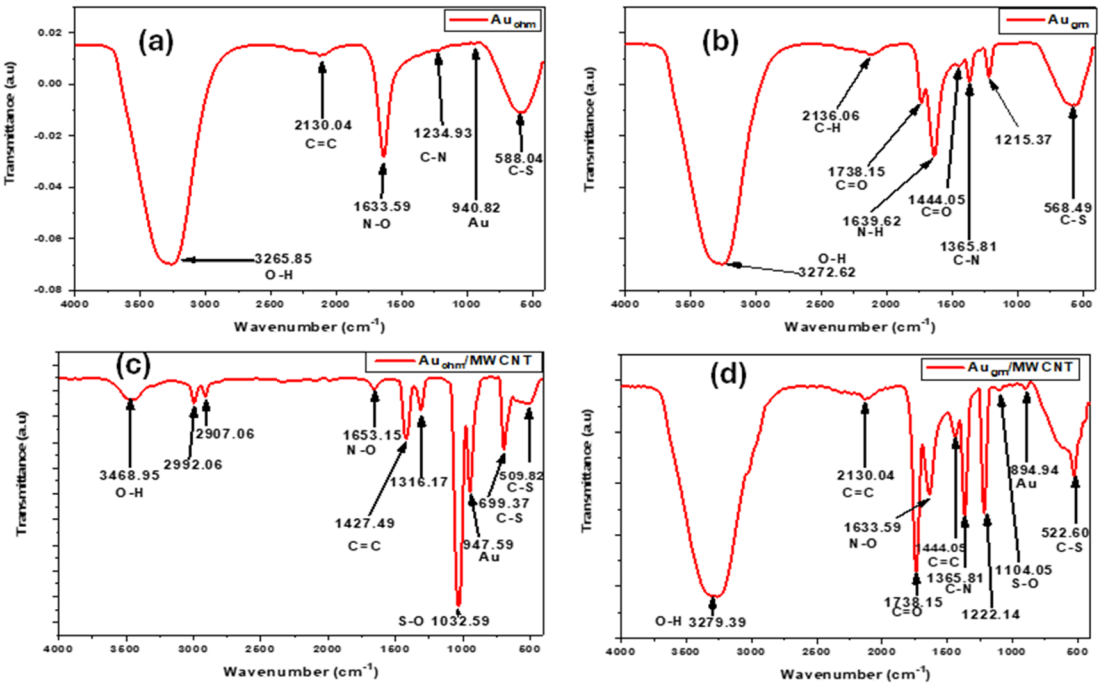

Fig. 2 The functional groups of (a) Au_{chm}, (b) Au_{grn}, (c) Au_{chm}/MWCNTs, and (d) Au_{grn}/MWCNTs in FTIR spectra.

groups, 1215.37, 1365.81, and 1639.62 cm^{-1} indicating the N–H stretch, which represents the presence of amino group and proteins, 1444.05 cm^{-1} indicating aromatic rings' C=C stretching, 1738.15 cm^{-1} indicating C=O from carbonyl groups such as ketones, aldehydes, and carboxylic acids from the *Hypoxis hemerocallidae corm* plant extract, and 3272.62 cm^{-1} attributed to O–H stretching indicating the presence of phenolics or alcoholic compounds.[88–90] Fig. 2(c) and (d) show peaks at 1540.90, 1788.78, and 2340.35 cm^{-1}, which are for C=C representing the presence of sp^2-hybridized carbons, C=O, and O–H introduced by the functionalization of MWCNTs to alter the properties of carbon-based materials.[70,91,92] Fig. 2(c) and (d) show proper synthesis of both green and chemically synthesized Au/MWCNTs, including O–H, which plays a significant role in facilitating electron transfer, stabilizing and dispersing Au on the surface of MWCNTs preventing aggregation, and also bonding with the nitrogen atom in MB dye increasing the adsorption of MB on the Au/MWCNT surface.[93,94] According to the literature, the Fermi level difference between AuNPs and MWCNTs drives spontaneous electron transfer from AuNPs to MWCNTs.[82] This redistribution reduces the surface charge of AuNPs, destabilizing citrate ions (which act as capping agents) and leading to their partial desorption (ions become desorbed when destabilized).[95] Since citrate contributes O–H groups *via* its carboxylate structure, this desorption directly reduces the OH group intensity and hence the reduction in the intensity of the O–H peak of Au_{chm}/MWCNTs.

3.3 XRD

The crystallite size of the synthesized nanoparticles was meticulously examined using X-ray diffraction (XRD) spectroscopy. The corresponding XRD patterns are presented in Fig. 3(a) and (b), showcasing the distinct diffraction peaks characteristic of the face-centered cubic (fcc) lattice structure. Specifically, the diffraction peaks at 38.22, 44.30, 64.59, and 77.50° for Au_{chm} and those at 38.69, 44.84, 64.98, and 77.97° for Au_{grn} were indexed to the (111), (200), (220), and (311) planes, respectively.[96,97] Previous work done on Ag/MWCNTs reported that prominent peaks for MWCNTs were observed at $2\theta = 25.70°$ (002) and 42.96° (100).[70] Au_{grn} showed better crystallinity in XRD peaks, and this is attributed to the presence of phenolics from the *Hypoxis hemerocallidae corm* plant extract, as observed by the intense O–H peak in Fig. 2(b) and (c), which are not present in TSC and $NaBH_4$ (phenolics) used in Au_{chm} synthesis.[98,99] Upon decorating MWCNTs with AuNPs, the resulting nanocomposites, Au_{chm}/MWCNTs and Au_{grn}/MWCNTs, retained the characteristic peaks of Au_{chm}, Au_{grn}, and MWCNTs, with the notable exception of the 25.70° (100) peak. Utilizing the Debye–Scherrer formula, eqn (1), the average crystallite size of the AuNPs was calculated, providing valuable insights into the structural properties of the nanoparticles.[100] A comprehensive analysis of the XRD results revealed distinct variations in particle size, crystallinity, and lattice structure among the green synthesized AuNPs, chemically synthesized AuNPs, and their respective nanocomposites with MWCNTs. Notably, the green synthesized AuNPs exhibited sharper and more pronounced peaks, indicative of high crystallinity and a narrow particle size distribution, with 8.698 nm particle size. In contrast, the incorporation of MWCNTs into the green synthesized AuNPs resulted in a subtle peak shift to the right, suggesting a slight decrease in particle size or lattice contraction, accompanied by a decrease in crystallinity, as evidenced by smaller peaks, with a calculated particle size of 17.089 nm.[70,101,102] Conversely, the chemically synthesized AuNPs displayed sharper peaks,

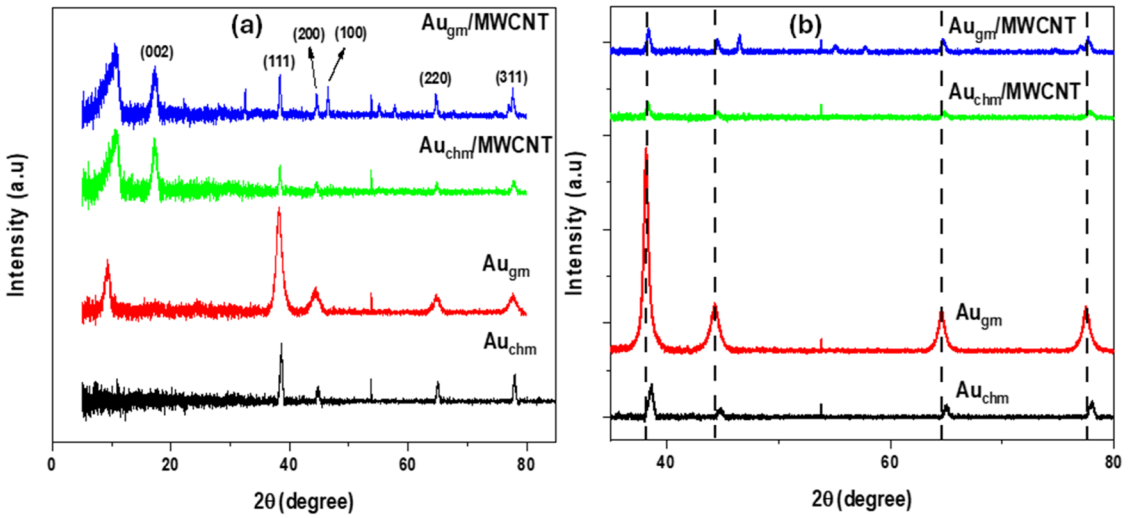

Fig. 3 XRD diffractograms of (a) Au_{chm}, Au_{grn}, MWCNTs, Au_{chm}/MWCNTs, and Au_{grn}/MWCNTs. (b) Magnified view of (a) from 35 to 80°.

characteristic of high crystallinity, with a larger particle size of 21.266 nm. Upon addition of MWCNTs, the particle size decreased to 18.73 nm, accompanied by a peak shift to the left, indicating lattice expansion, and a decrease in crystallinity, as manifested by shorter peaks.[70,103,104] These findings unequivocally demonstrate that the incorporation of MWCNTs influences the particle size and crystallinity of AuNPs, with varying effects depending on the synthesis method.

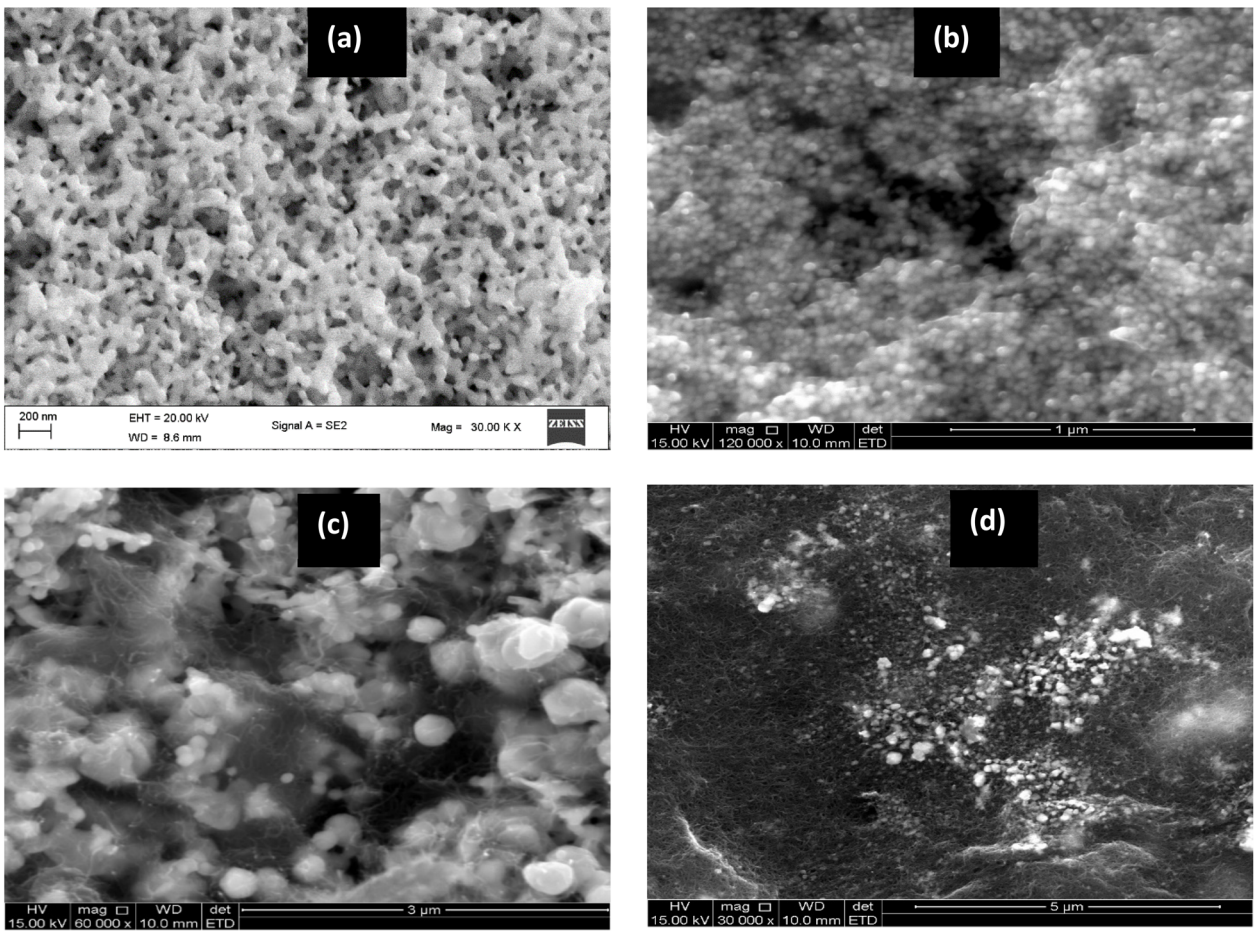

Fig. 4 SEM images of (a) Au_{chm}, (b) Au_{grn}, (c) Au_{chm}/MWCNTs, and (d) Au_{grn}/MWCNTs.

$$D = \frac{K\lambda}{\beta \cos \theta} \quad (1)$$

where D is the average crystallite size (nm), K is the shape factor, λ is the wavelength of X-rays (nm), β is the full width at half-maximum (FWHM) of peak (radians), and θ is the Bragg angle (degrees).

3.4 SEM results

Fig. 4 presents the SEM images of Au/MWCNT nanocomposites and their pristine nanoparticles. Fig. 4(a) shows agglomerated spherical structures that were a bit flake-like produced by the chemical reduction method using trisodium citrate dihydrate and sodium borohydride. The non-uniform, rough-surfaced AuNPs with intersections and varying nanogaps may outperform spherical and clustered nanoparticles due to enhanced hotspots and effective LSPR–LSPR coupling, beneficial for sensing and SERS applications. This unique morphology creates plentiful hotspots, increasing local electromagnetic fields and potentially leading to improved performance.[105] In contrast, Fig. 4(b) shows agglomerated spherical structures, which enhance the sensor performance by their excellent conductivity, high surface area, electrocatalytic properties, stability, and durability. Their spherical shape allows uniform film formation, improving reproducibility and signal uniformity.[47,48,106–108] Fig. 4(c) depicts a combination of agglomerated spherical flake-like structures and tanged tubular structures, while Fig. 4(d) shows less agglomerated spherical structures spread across the surface of MWCNT tubular structures. MWCNTs show tangled tubular structures similar to the ones found in the literature.[109] The aggregation of Au_{chm} on the surface of MWCNTs can reduce the number of electrochemically active sites, leading to decreased catalytic activity towards MB detection. This aggregation also compromises the stability, electron transfer, and dispersibility, ultimately affecting the overall performance of the sensor.[110] This shows that Au_{grn}/

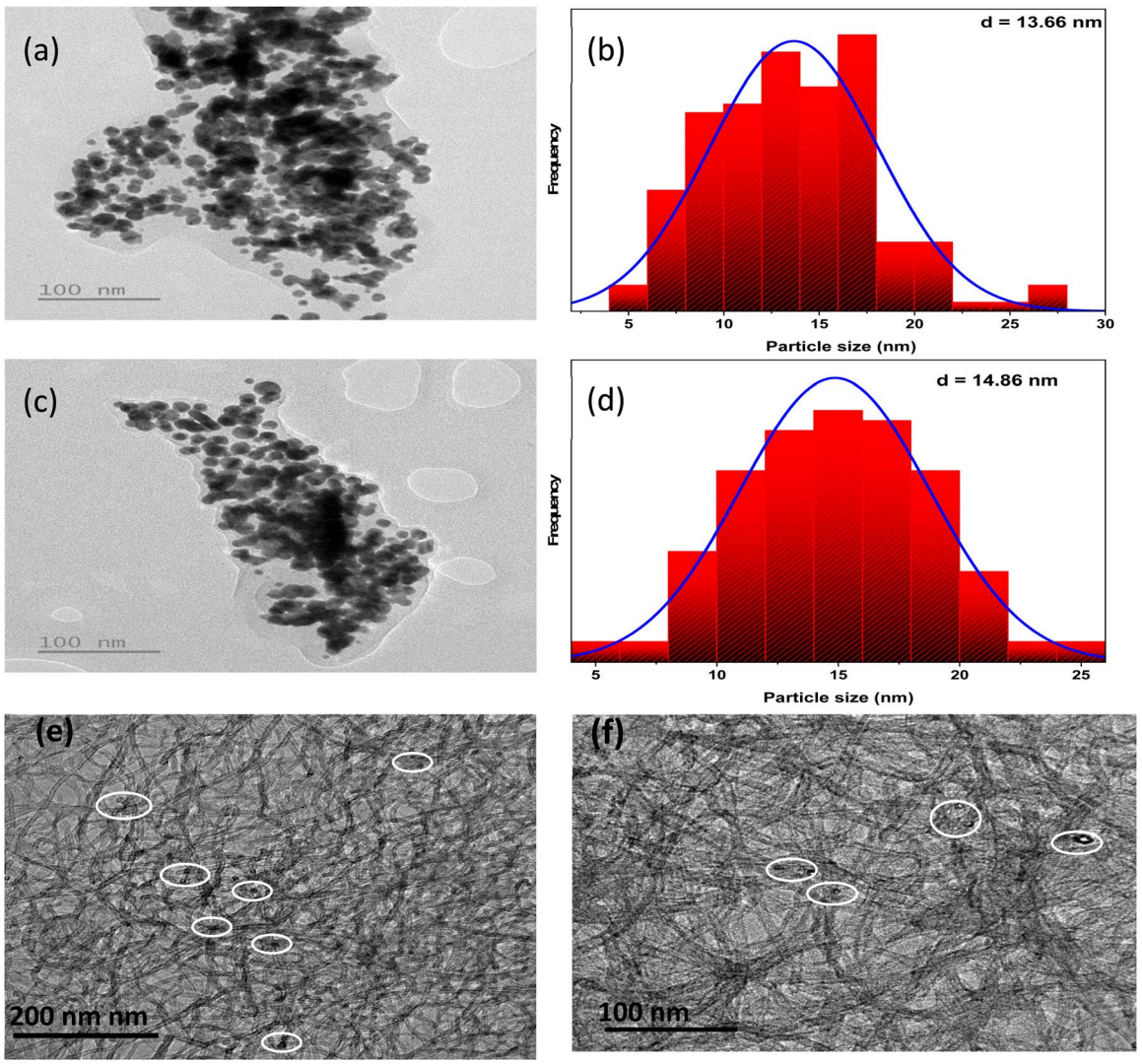

Fig. 5 The TEM images of (a) Au_{chm}, (c) Au_{grn}, (e) Au_{chm}/MWCNTs, and (f) Au_{grn}/MWCNTs. The average particle size histograms of (b) Au_{chm} and (d) Au_{grn}.

MWCNTs has a possibility of outperforming Au_{chm}/MWCNTs due to less aggregation of Au_{grn} on the surface of MWCNTs, due to enhanced transfer of electrons between the analyte and the electrode due to increased electrode surface area.[111]

3.5 TEM analysis

Transmission Electron Microscopy (TEM) was employed to determine the particle size and observe the morphology of the nanoparticles. The TEM images in Fig. 5(a) and (c) reveal that Au_{chm} and Au_{grn} nanoparticles exhibit spherical shapes, with average particle sizes of 13.66 nm and 14.86 nm, respectively. Fig. 5(e) and (f) display the TEM images of Au_{chm}/MWCNT and Au_{grn}/MWCNT nanocomposites, where AuNPs are highlighted with red circles, indicating successful decoration of AuNPs on the MWCNT surface. The AuNPs are evenly distributed among the tangled MWCNT structures, suggesting a good interaction between the AuNPs and MWCNTs. This uniform distribution is crucial for enhancing the electrochemical performance of the nanocomposites. The TEM analysis provides valuable insights into the structural characteristics of nanoparticles and nanocomposites, which is essential for understanding their electrochemical behaviour.

3.6 Voltammetry studies

3.6.1 Electrode optimization studies. Optimization and characterization of Au : MWCNT nanocomposite electrodes were performed to identify the optimal Au : MWCNTs ratio and investigate their electrochemical properties in 5 mM $[Fe(CN)_6]^{3-/4-}$. Cyclic voltammetry (CV) studies were conducted at three different ratios for both Au_{chm}/MWCNT and Au_{grn}/MWCNT nanocomposites. The redox probe was prepared in 0.1 M phosphate buffer (PB) solution at pH 7. The highest current response was exhibited by the 1 : 3 ratio for the chemically synthesized nanocomposite (Fig. 6(a) and (b)) and 1 : 2 ratio for the green synthesized nanocomposite (Fig. 6(c) and (d)).

For electron transfer properties and electrochemical efficiency, CV was used in 5 mM $[Fe(CN)_6]^{3-/4-}$ to investigate the properties of Au_{chm}/MWCNTs and Au_{grn}/MWCNTs over the potential range of −0.4 to 0.8 V. The scan rate was set at 25 mV s^{-1}. In Fig. 7(a) and (b), the anodic peaks showed a decreasing current response in the following order: Au_{chm}/MWCNTs (415.591 μA) > Au_{grn}/MWCNTs (244.539 μA) > MWCNTs (190.464 μA) > bare (36.538 μA) > Au_{grn} (18.401 μA) > Au_{chm} (4.507 μA). Notably, the current response of Au_{grn} and Au_{chm} was lower than that of the bare electrode, indicating poor conductivity. However, their nanocomposites exhibited significantly higher current responses, demonstrating improved electrochemical performance due to the high electric conductivity and larger surface area of MWCNTs.[109,112] The electrochemical reversibility of the electrodes was evaluated based on the I_{pa}/I_{pc} values and ΔE_p values listed in Table 1. The results show that the reactions were nearly reversible for bare, MWCNTs, Au_{chm}/MWCNTs, and Au_{grn}/MWCNTs, with I_{pa}/I_{pc} values of 0.899, 0.975, 1.067, and 1.155, respectively. In contrast, Au_{chm} exhibited high irreversibility with an I_{pa}/I_{pc} value of 3.558. The ΔE_p values greater than 57 mV further supported the conclusion that the reactions were

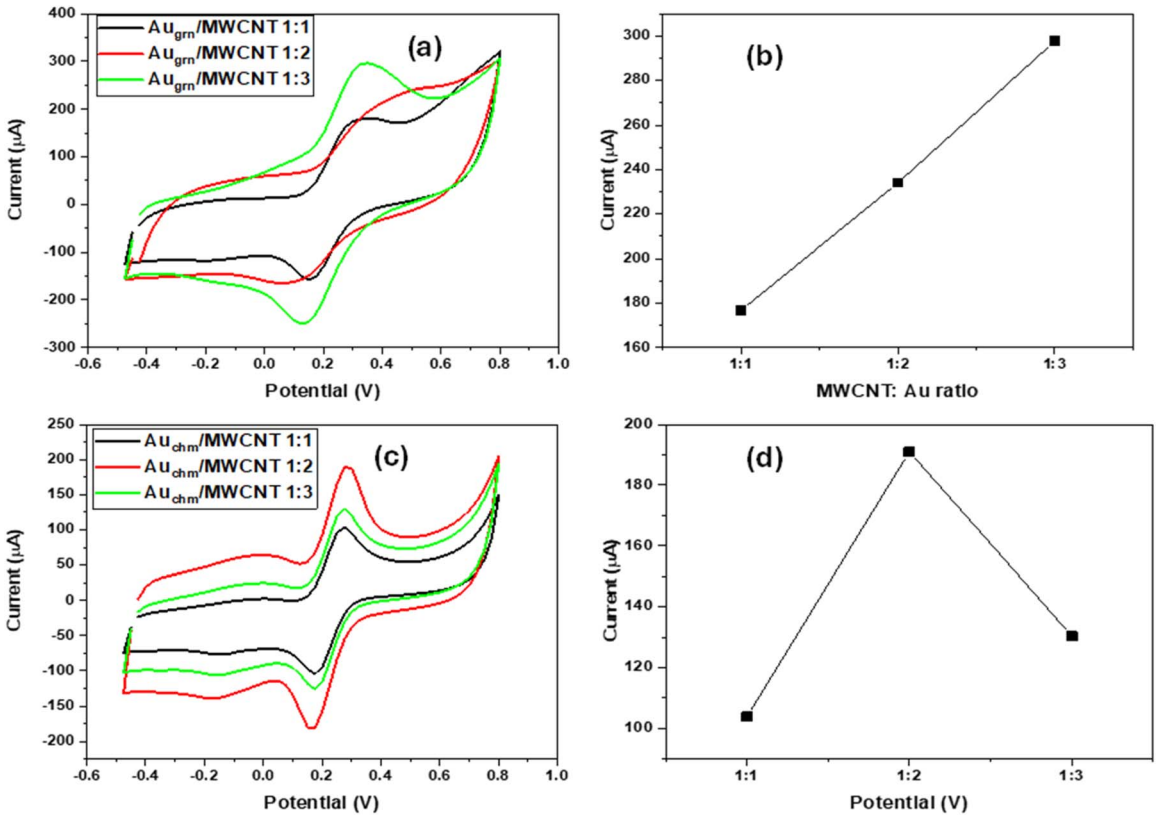

Fig. 6 Electrode optimization study of (a and b) Au_{chm} : MWCNT and (c and d) Au_{grn} : MWCNT.

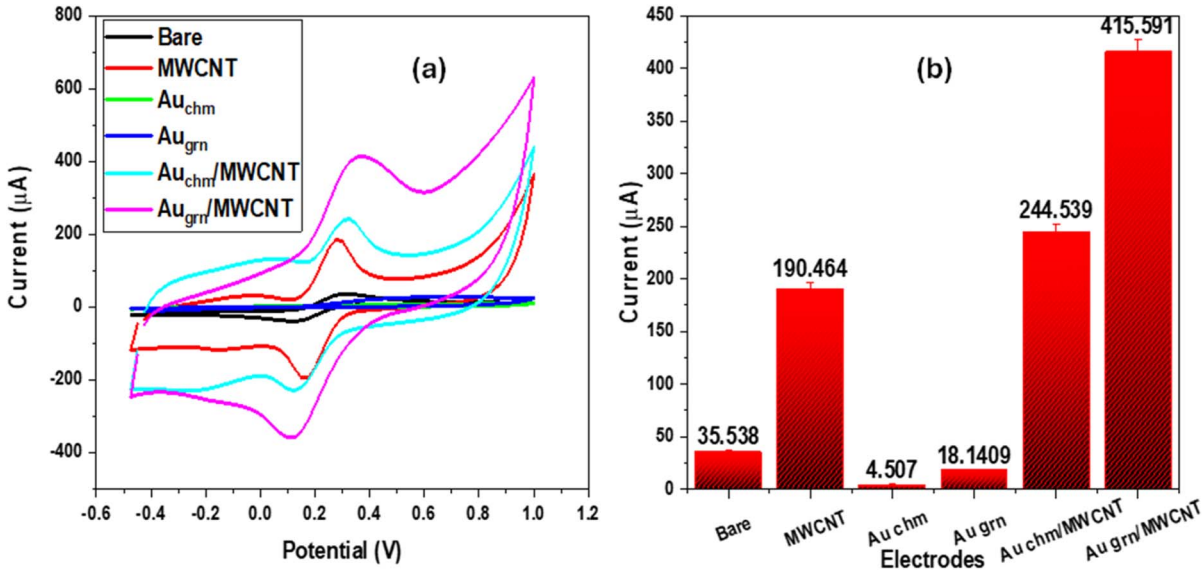

Fig. 7 CV of (a) bare, MWCNT, Au_{chm}, Au_{grn}, MWCNT, Au_{chm}/MWCNT, and Au_{grn}/MWCNT in 5 mM $[Fe(CN)_6]^{3-/4-}$. (b) Bar graph of oxidation peaks of all electrodes.

Table 1 Comparative evaluation of the electrochemical behaviour of modified and unmodified electrodes in the redox probe

Electrode	I_{pa} (μA)	I_{pc} (μA)	I_{pa}/I_{pc} (μA)	E_{pa} (V)	E_{pc} (V)	ΔE_p (V)
Bare	35.538	−39.531	−0.899	0.312	0.122	0.217
MWCNTs	190.464	−195.264	−0.975	0.281	0.159	0.220
Au_{chm}	4.507	−1.265	−3.558	0.350	0.156	0.253
Au_{grn}	18.141	—	—	0.554	—	0.277
Au_{chm}/MWCNTs	244.539	−229.156	−1.067	0.317	0.117	0.217
Au_{grn}/MWCNTs	415.591	−359.847	−1.155	0.356	0.110	0.233

nearly reversible for the nanocomposites.[70,113] Eqn (2) was used to calculate the EASA, which is an effective electroactive surface area. The results showed that the EASA values were 0.053, 0.031, 0.024, 0.006, 0.005, and 0.002 cm^2 for Au_{chm}/MWCNTs, Au_{grn}/MWCNTs, MWCNTs, Au_{grn}, bare, and Au_{chm}, respectively. The nanocomposites exhibited larger EASA values compared to their pristine nanoparticles, demonstrating the benefits of decorating the surface of MWCNTs, and the synergistic properties

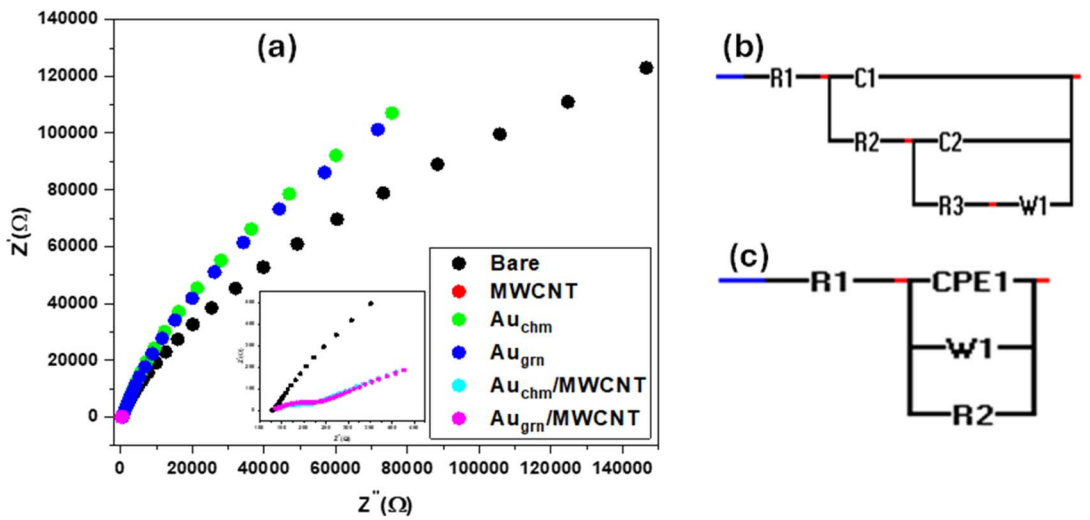

Fig. 8 (a) Nyquist plot of all the nanomaterials and (b and c) equivalent circuit models.

coming from the combination of MWCNTs and AuNPs. Overall, characterization studies demonstrated improved electrochemical performance and increased EASA for the Au/MWCNT nanocomposites.

$$I_p = 2.69 \times 10^5 n^{3/2} A D^{1/2} C v^{1/2} \quad (2)$$

The variables used in the calculation are: A (effective electroactive surface area in cm^2), C ($[Fe(CN)_6]^{3-}/^{4-}$ concentration in mol cm^{-3}), D (diffusion coefficient in $cm^2\ s^{-1}$), n (number of transferred electrons), v (scan rate in V s^{-1}), and I_p (anodic peak current in A).[70]

3.6.2 Electrochemical impedance spectroscopy studies. Electrochemical impedance spectroscopy (EIS) was used to determine the sensor properties of all nanomaterials, including the bare electrode, in 5 mM $[Fe(CN)_6]^{3-/4-}$ at 0.3 V. Fig. 8(b) and (c) show the two equivalent circuits used to fit the Nyquist plot in Fig. 8(a). The circuit parameters include a constant phase element (CPE), solution resistance (R_s), capacitance (C), charge transfer resistance (R_{ct}), Warburg impedance (W), resistance (R), and the chi-squared value (χ^2). According to Table 2, the R_{ct} values follow the trend: 32.20 Ω < 34.02 Ω < 36.61 Ω < 3.4×10^5 Ω < 3.7×10^5 Ω < 5.6×10^5 Ω for Au_{grn}/MWCNTs, MWCNTs, Au_{chm}/MWCNTs, Au_{chm}, Au_{grn}, and bare electrode, respectively. Notably, the R_{ct} trend generally correlates with the increase in current response observed in Fig. 7 in FeCN, except for the bare electrode. The bare electrode's deviation from the trend may be attributed to its instability due to the lack of modification. The

Table 2 Fitted circuit data of all electrodes

Electrodes	Bare	MWCNTs	Au_{chm}	Au_{grn}	Au_{chm}/MWCNTs	Au_{grn}/MWCNTs
R_s (Ω)	437.8	128.54	502.52	505.62	136.27	134.94
R_{ct} (Ω)	5.6×10^5	34.02	3.7×10^5	3.4×10^5	36.61	32.20
R (Ω)	—	80.05	—	—	35.46	55.17
C_1	—	2.8×10^4	—	—	3.8×10^4	2.8×10^4
C_2	—	3.5×10^4	—	—	2.4×10^4	1.6×10^4
CPE (F)	1.9×10^{-6}	—	8.9×10^{-6}	9.6×10^{-6}	—	—
n	0.87	—	0.81	0.82	—	—
W (F)	1.8×10^5	845	1×10^7	1×10^7	250.36	267.64
X^2	0.003904	0.000165	0.040212	0.004587	0.000295	0.000581

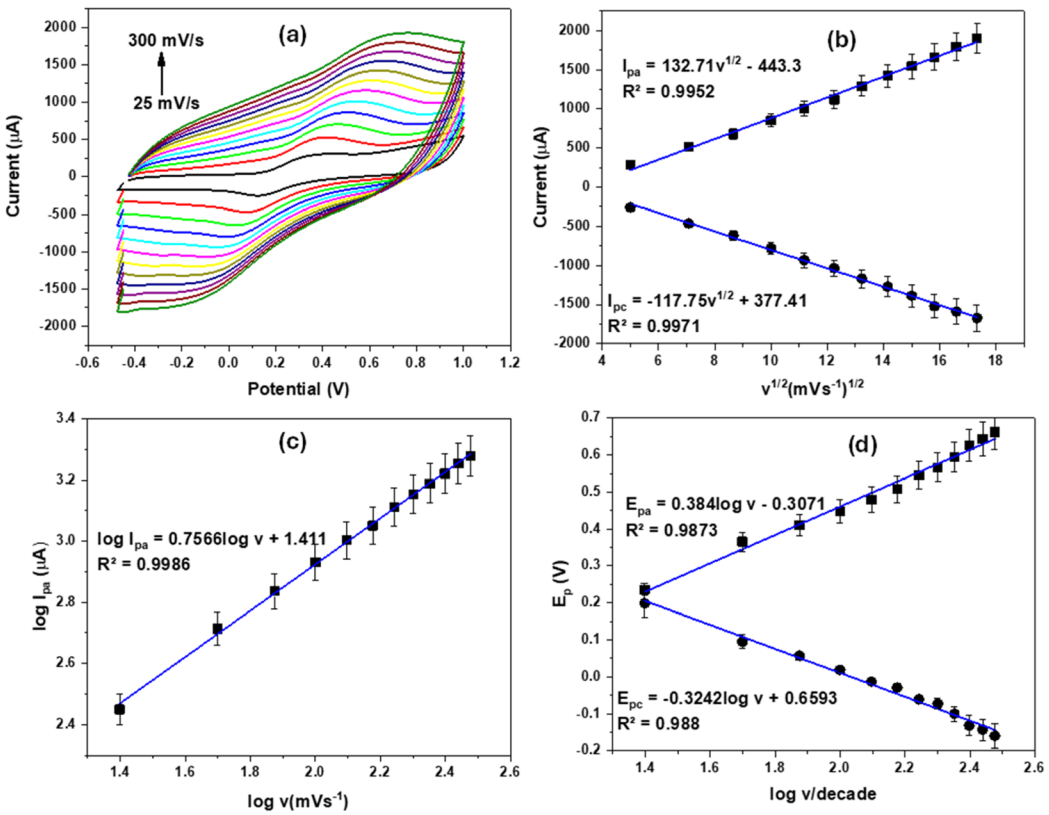

Fig. 9 (a) The scan rate of Au_{chm}/MWCNTs, (b) I_p *vs.* v^2, (c) log I_{pa} *vs.* log v, and (d) E_p *vs.* log v in 5 mM $[Fe(CN)_6]^{3-/4-}$.

EIS data for Au_{grn}/MWCNTs, Au_{chm}/MWCNTs, and MWCNTs were fitted using the circuit in Fig. 8(b), which includes the double capacitance. In contrast, the bare electrode, Au_{chm}, and Au_{grn} were fitted using the circuit in Fig. 8(c), which includes a CPE instead of C, with n-values of approximately 0.8, indicating non-ideal capacitive behaviour due to the electrode surface's inhomogeneity. The higher n-value for the bare electrode, closer to 1, may also influence its behaviour compared to Au_{chm} and Au_{grn}.[70] The low χ^2 values indicate the excellent fit of the data to the corresponding EIS circuits.

3.6.3 Scan rate studies. The influence of scan rate on the electrochemical response of Au_{chm}/MWCNTs and Au_{grn}/MWCNTs was investigated using CV in a potential window of −0.4 to 1 V to give insight into electrode catalytic activity, electron transfer kinetics, and surface redox processes at the scan rate of 25 mV s^{-1} in 5 mM $[Fe(CN)_6]^{3-/4-}$, which was prepared in phosphate buffer solution of 0.1 M concentration. The chemically synthesized Au/MWCNT nanocomposite exhibited a directly proportional relationship between the peak current (I_p) and the scan rate (v), as observed in Fig. 9(a), indicating a surface-controlled electrochemical process. However, the broad and flat peaks suggest a slow electron transfer kinetics, which may be attributed to the high electron transfer resistance at the electrode–electrolyte interface.[114] The anodic and cathodic peak potentials given by eqn (6) and (7) in Fig. 9(d) (E_{pa} = 0.659 V and E_{pc} = −0.7747 V) indicate a large overpotential, which may be due to the sluggish electron transfer kinetics. The coefficient of electron transfer (α) was determined to be 0.462, calculated using equations outlined in eqn (8) and (9), indicating a quasi-reversible electron transfer process. The $\log I_{pa}$ *vs.* $\log v$ plot's gradient (0.7566) deviates from 0.5 (theoretical value), which indicates a mixed diffusion–adsorption control. This suggests that both diffusion and adsorption processes influence the electrochemical reaction.[113] Furthermore, the Tafel slope (b) was calculated using eqn (10) and was found to be 0.335 V, which indicates a high electron transfer resistance and a slow electron transfer kinetics.

$$I_{pa} = 132.71v^{1/2} - 443.3 \quad (R^2 = 0.995) \tag{3}$$

$$I_{pc} = -117.75v^{1/2} + 377.41 \quad (R^2 = 0.9971) \tag{4}$$

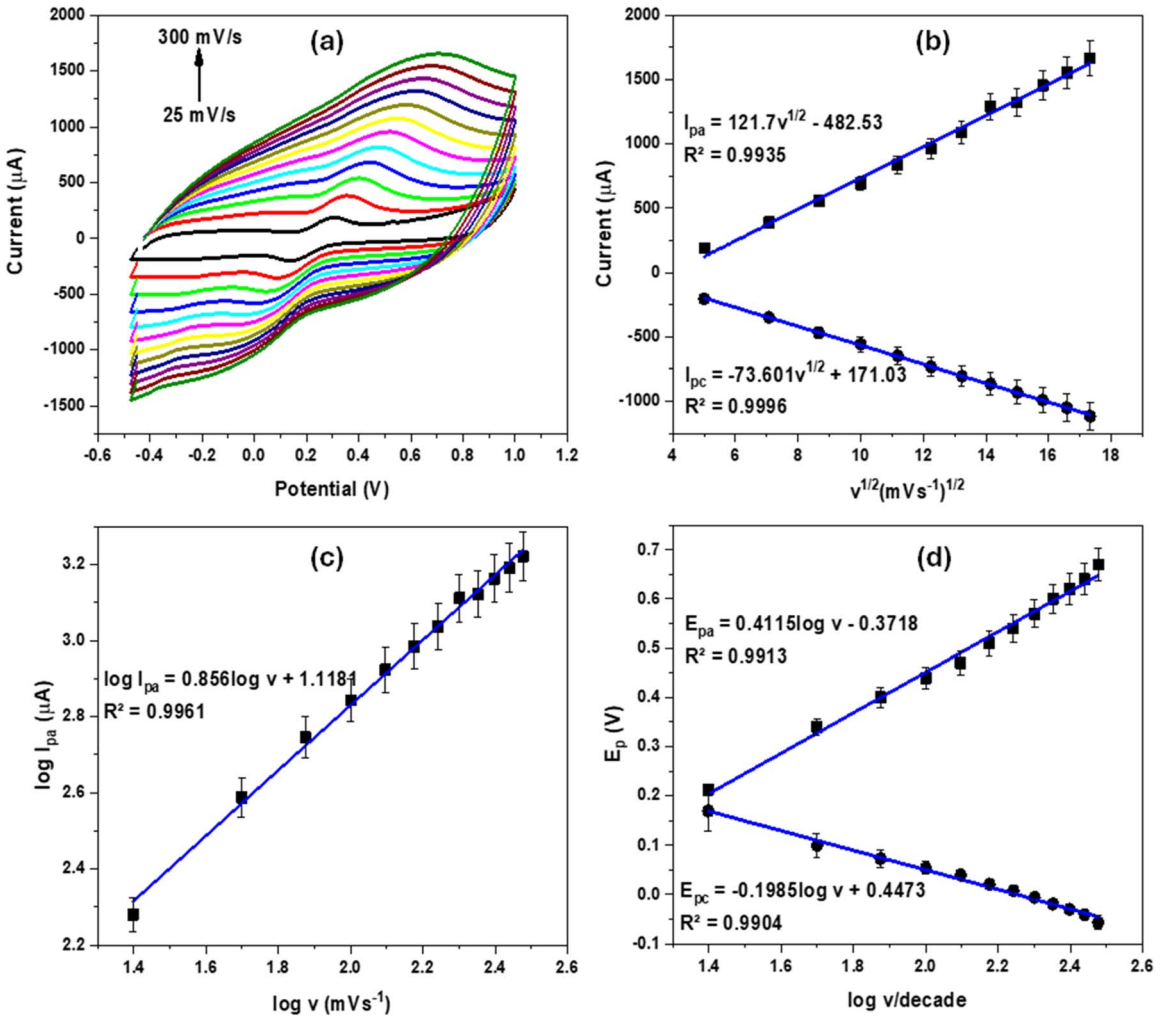

Fig. 10 (a) The scan rate of Au_{grn}/MWCNTs, (b) I_p *vs.* v^2, (c) $\log I_{pa}$ *vs.* $\log v$, and (d) E_p *vs.* $\log v$ in 5 mM $[Fe(CN)_6]^{3-/4-}$.

$$\log I_{pa} = 0.7566 \log v + 1.411 \quad (R^2 = 0.9986) \tag{5}$$

$$E_{pa} = 0.669 \log v - 0.2389 \quad (R^2 = 0.9759) \tag{6}$$

$$E_{pc} = -0.7747 \log v + 0.2723 \quad (R^2 = 0.9832) \tag{7}$$

$$E_{pa} = E^0 + \frac{2.303RT}{(1-a)nF} \log v \tag{8}$$

$$E_{pc} = E^0 - \frac{2.303RT}{anF} \log v \tag{9}$$

$$E_p = \text{constant} + \left(\frac{b}{2}\right) \log v \tag{10}$$

In contrast, the green synthesized Au/MWCNT nanocomposite also exhibited that the peak current (I_p) and the scan rate (v) have a directly proportional relationship, as observed in Fig. 10(a), but with a more pronounced adsorption-controlled behaviour. The anodic peak potential given by eqn (11) and (12) is for the cathodic peak potential in Fig. 10(d) ($E_{pa} = 0.4115$ V and $E_{pc} = -0.1985$ V), indicating a lower overpotential compared to the chemically synthesized nanocomposite, suggesting faster electron transfer kinetics. The electron transfer coefficient (α) was determined to be 0.22, calculated using equations outlined in eqn (8) and (9), indicating a more irreversible electron transfer process. The gradient of the $\log I_{pa}$ against $\log v$ plot was found to be 0.856, which deviates significantly from 0.5, indicating a pure adsorption-controlled process. The Tafel slope (b) was calculated to be 0.206 V, which indicates a relatively lower electron transfer resistance and a faster electron transfer kinetics compared to the chemically synthesized nanocomposite.

$$I_{pa} = 121.71 v^{1/2} - 482.53 \quad (R^2 = 0.9935) \tag{11}$$

$$I_{pc} = -73.601 v^{1/2} + 171.03 \quad (R^2 = 0.9996) \tag{12}$$

$$\log I_{pa} = 0.856 \log v + 1.1181 \quad (R^2 = 0.9961) \tag{13}$$

$$E_{pa} = 0.4115 \log v - 0.3918 \quad (R^2 = 0.9913) \tag{14}$$

$$E_{pc} = -0.1985 \log v + 0.4473 \quad (R^2 = 0.9904) \tag{15}$$

The heterogeneous electron transfer constant (k_s) was calculated for both Au_{chm}/MWCNTs and Au_{grn}/MWCNTs using eqn (16) and were found to be 0.00415 cm s^{-1} and 0.00142 cm s^{-1}, respectively, which are relatively low, indicating a slow electron transfer rate.

$$\log k_s = a \log(1-a) + (1-a) \log a - \log \frac{RT}{nF} - a(1-a) \frac{nF\Delta E_p}{2.303RT} \tag{16}$$

3.6.4 Catalysis. Electrochemical properties of all the electrodes towards detecting 0.1 mM MB dye that was prepared at a pH of 5 in 0.1 M HCl were investigated in the potential range of −0.4 to 1.0 V using a CV technique at a scan rate of 25 mV s^{-1}. The oxidation current response decreases in the order of 124.29 μA, 114.77 μA, 60.85 μA, 18.96 μA, 2.81 μA, and 2.08 μA for MWCNT, Au_{grn}/MWCNTs, Au_{chm}/MWCNTs, Au_{chm}, bare, and Au_{grn}, respectively, as displayed in Fig. 11(a) and (b). MWCNTs showed the highest current response, indicating that it has better electrochemical properties towards MB detection. The electrochemical analysis revealed that the I_{pa}/I_{pc} values of 0.463 μA, 0.925 μA, 0.299 μA, 0.861 μA, and 0.871 μA for the bare, MWCNT, Au_{grn}, Au_{chm}/MWCNT, and Au_{grn}/MWCNT electrodes, respectively, indicating that the MWCNT electrode exhibits a nearly reversible electrochemical reaction.[115] In contrast, the other electrodes show quasi-reversible behaviour. ΔE_p values in Table 3 are as follows: 0.262, 0.128, 0.429, 0.519, and 0.374 V for the respective electrodes suggest that the MWCNT electrode has the fastest electron transfer kinetics, while the Au_{chm}/MWCNT

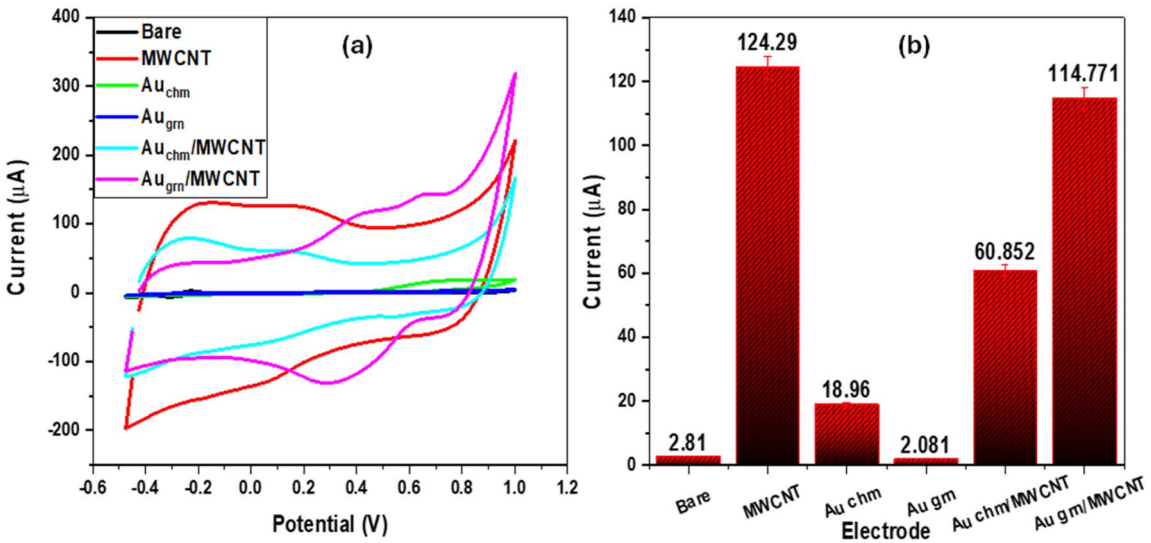

Fig. 11 CV of (a) bare, MWCNTs, Au_{chm}, Au_{grn}, MWCNTs, Au_{chm}/MWCNTs, and Au_{grn}/MWCNTs in MB (0.1 mM). (b) Bar graph of oxidation peaks of modified and unmodified electrodes.

Table 3 Comparative evaluation of the electrochemical behaviour of modified and unmodified electrodes in MB

Electrode	I_{pa} (μA)	I_{pc} (μA)	I_{pa}/I_{pc} (μA)	E_{pa} (V)	E_{pc} (V)	ΔE_p (V)
Bare	2.81	−6.078	0.463	−0.225	−0.299	0.262
MWCNTs	124.29	−134.304	0.925	0.218	0.0381	0.128
Au_{chm}	18.96	—	—	0.772	—	0.386
Au_{grn}	2.081	−6.967	0.299	0.532	0.327	0.429
Au_{chm}/MWCNTs	60.852	−70.632	0.861	0.177	0.0757	0.519
Au_{grn}/MWCNTs	114.771	−131.735	0.871	0.431	0.317	0.374

electrode has the slowest kinetics. The poor performance of Au_{chm}/MWCNTs compared to Au_{grn}/MWCNTs can be attributed to the aggregation of AuNPs on the electrode surface, reducing active sites on MWCNTs for interaction with MB. Additionally, the Aug/MWCNT electrode's intense OH peak suggests a higher density of hydroxyl groups (possibly from COOH) on its surface, which may have enhanced its interaction with MB, contributing to its better performance. Notably, the Au_{chm} electrode exhibits an irreversible electrochemical reaction, characterized by the presence of only an oxidation peak and the absence of a reduction peak, suggesting a rate-limiting process at the electrode surface (kinetically limited). The ΔE_p value of 0.386 for Au_{chm} further supports this interpretation, since a larger ΔE_p value close to zero indicates a reversible or Nernstian behaviour, while a larger ΔE_p value indicates a more irreversible or kinetically limited behaviour. A ΔE_p value of 0.386 is relatively large, indicating that the Au_{chm} electrode reaction is not reversible and is likely limited by kinetic factors, such as slow electron transfer or mass transport.[115] The superior kinetics of MWCNTs can be attributed to its high surface area, conductive network, fast electron transfer, and potential catalytic activity.[116,117] In contrast, the Au/MWCNT composite electrodes (Au_{chm}/MWCNT and Au_{grn}/MWCNT) exhibit reduced kinetics, likely due to the agglomeration of AuNPs on the MWCNT surface, as was observed in SEM images in Fig. 4 (c) and (d), which reduces the active surface area, increases electron transfer resistance, blocks conductive pathways, and decreases stability. This agglomeration might be responsible for the decreased electrochemical performance of the composite material compared to the pristine MWCNTs.[118–120]

3.6.5 Scan rate studies. The influence of scan rate on the electrochemical response of Au_{chm}/MWCNTs and Au_{grn}/MWCNTs was investigated using CV to give insight into electrode catalytic activity, electron transfer kinetics, and surface redox processes over a potential range of −0.4 to 1 using CV, operated at the scan rate of 25 mV s^{-1} in MB dye (0.1 mM). The chemically synthesized Au/MWCNT nanocomposite exhibited a directly proportional relationship between (I_p) and (ν), indicating that the electrochemical process is surface-controlled. The sharp anodic and cathodic peaks at $E_{pa} = 0.1034$ V and $E_{pc} = -0.0796$ V, respectively, from eqn (20) and (21) in Fig. 12(d) suggest a relatively fast electron transfer kinetics. 0.565 was the

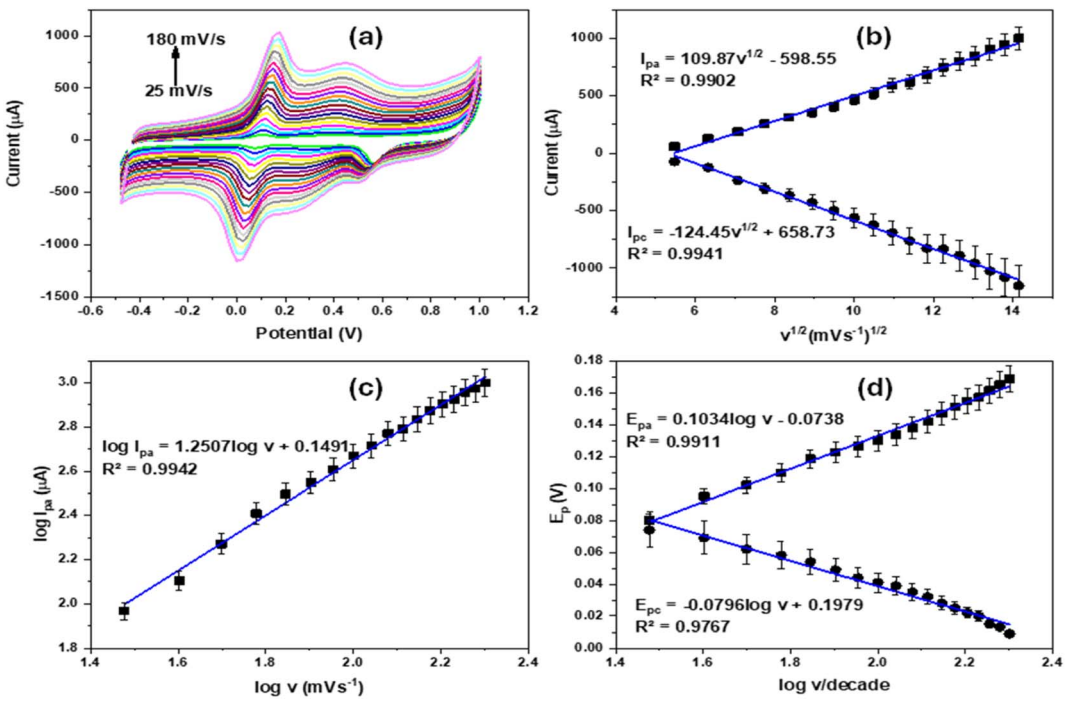

Fig. 12 (a) The scan rate of Au_{chm}/MWCNTs, (b) I_p *vs.* v^2, (c) log I_{pa} *vs.* log v, and (d) E_p *vs.* log v in 0.1 mM MB.

value determined for the electron transfer coefficient (α), indicating a quasi-reversible electron transfer process. The $\log I_{pa}$ *vs.* $\log v$ gradient (1.2507) deviates from 0.5, which indicates an adsorption control reaction process. However, the Tafel slope (b) was calculated using eqn (10) and was found to be 0.0516 V, which indicates a relatively low electron transfer resistance and a faster electron transfer kinetics. This suggests that adsorption processes primarily influence the electrochemical reaction.[70,113,114]

$$I_{pa} = 109.87v^{1/2} - 598.55 \quad (R^2 = 0.9902) \tag{17}$$

$$I_{pc} = -124.45v^{1/2} + 658.73 \quad (R^2 = 0.9941) \tag{18}$$

$$\log I_{pa} = 1.2507 \log v + 0.1491 \quad (R^2 = 0.9942) \tag{19}$$

$$E_{pa} = 0.1034 \log v - 0.0738 \quad (R^2 = 0.9911) \tag{20}$$

$$E_{pc} = -0.0796 \log v + 0.1979 \quad (R^2 = 0.9767) \tag{21}$$

In contrast, in Fig. 13(a), the green synthesized Au/MWCNT nanocomposite also exhibited a directly proportional relationship between (v) and (I_p) but with a more pronounced adsorption-controlled behaviour. As observed in Fig. 13(a) and (d), the sharp anodic peak at $E_{pa} = 0.094$ V, without a corresponding cathodic peak, suggests a relatively slow electron transfer kinetics. The coefficient of electron transfer (α) was calculated using eqn (25) and was found to be 0.226, indicating a more irreversible electron transfer process. The gradient of the $\log I_{pa}$ *vs.* $\log v$ plot (0.6992) deviates significantly from 0.5, which indicates a mixed diffusion and adsorption-controlled reaction process with dominant diffusion control. The Tafel slope (b) was calculated using eqn (10) and was found to be 0.046 V, which indicates a relatively low electron transfer resistance. However, the overall electrochemical performance of the green synthesized Au/MWCNT nanocomposite is lower compared to the chemically synthesized material.[70,113,114]

$$I_{pa} = 61.364v^{1/2} - 124.55 \quad (R^2 = 0.9985) \tag{22}$$

$$\log I_{pa} = 0.6992 \log v + 1.28057 \quad (R^2 = 0.9985) \tag{23}$$

$$E_{pa} = 0.094 \log v - 0.0346 \quad (R^2 = 0.9918) \tag{24}$$

$$\left|E_p - E_{1/2}\right| = \frac{47.7}{(1-a)}(\text{mV}) \tag{25}$$

3.6.6 Concentration studies. The electroanalytical detection of MB dye was performed over a potential range of 0 to 0.9 V using SWV. Concentrations varied from 19.08 nM to 116.53 nM. The sensitivity of Au-MWCNT nanocomposite-modified electrodes towards MB dye was evaluated in 0.1 M HCl at a pH of 5. Fig. 14(a) shows that the current response of the Au_{chm}/MWCNT electrode exhibited a positive correlation with increasing MB

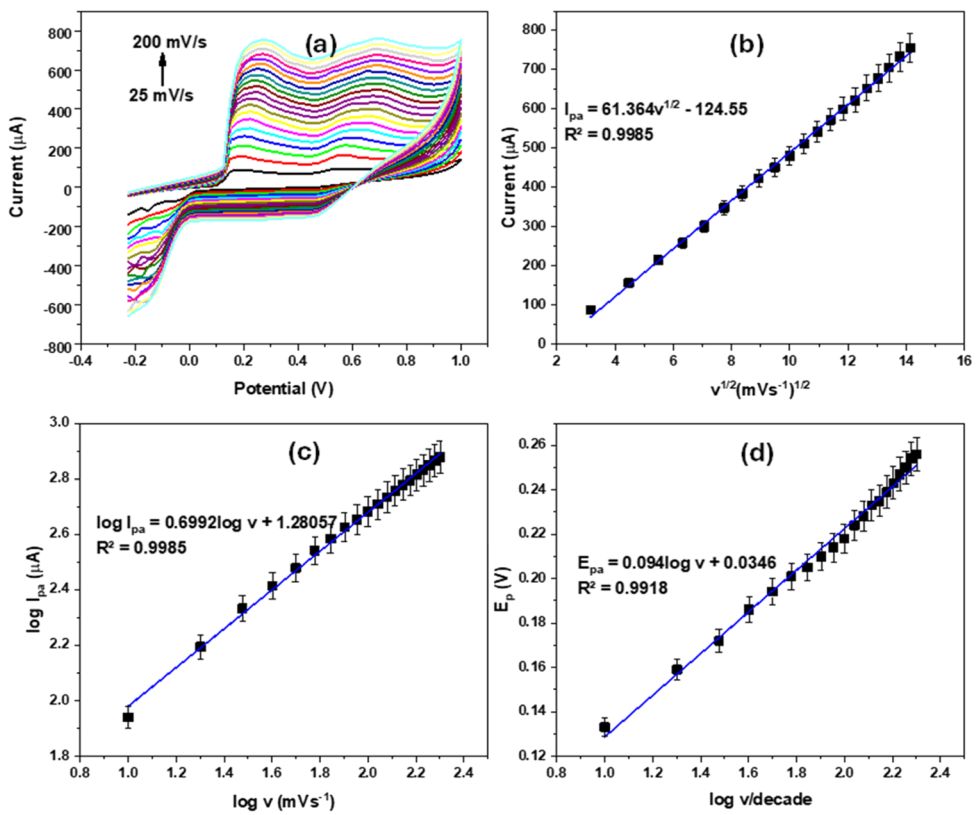

Fig. 13 (a) The scan rate of Au_{grn}/MWCNTs, (b) I_p *vs.* v^2, (c) $\log I_{pa}$ *vs.* $\log v$, and (d) E_p *vs.* $\log v$ in 0.1 mM MB.

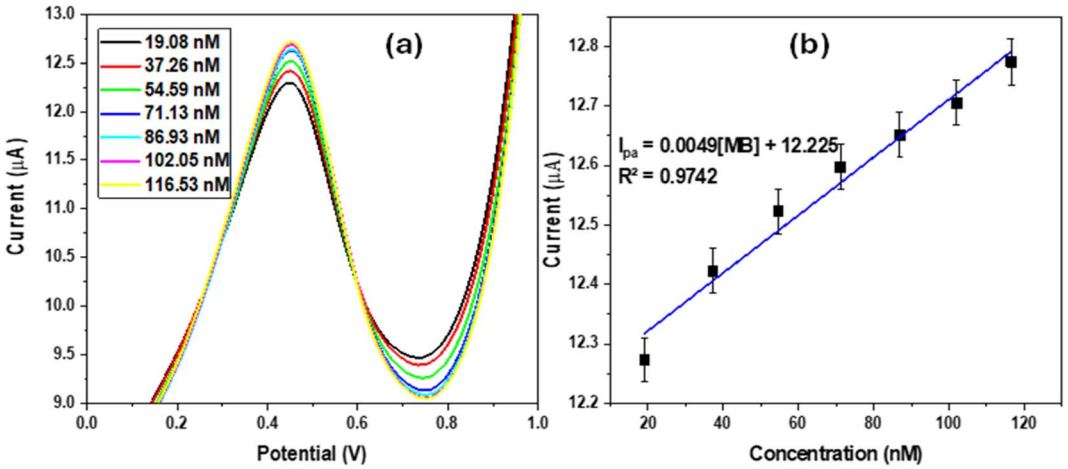

Fig. 14 (a) SWV of Au_{chm}/MWCNTs in MB concentration ranging from 19.08 to 116.53 nm and (b) Au_{chm}/MWCNT linear plot of I_p *vs.* conc.

dye concentrations, whereas, in Fig. 15(a), the Au_{grn}/MWCNT electrode displayed an inverse relationship between the concentration and current response. This phenomenon can be attributed to the predominantly adsorption-controlled behaviour of the Au_{grn}/MWCNT electrode, where the dye molecules adsorb onto the electrode surface until saturation is reached, resulting in a decrease in current response.[70] The Au_{grn}/MWCNT electrode's predominantly adsorption-controlled behaviour in FeCN (slope: 0.856) and mixed diffusion–adsorption control with diffusion dominating in MB (slope: 0.6992) likely led to saturation of active sites at higher MB concentrations, resulting in a mass transfer peak current limit (decreasing current with increasing concentration).[70] Au_{chm}/MWCNT electrode's mixed diffusion–adsorption control in FeCN (slope: 0.7566) and purely adsorption-controlled behaviour in MB (slope: 1.2507) allowed for a more efficient interaction between the analyte and electrode, resulting in an increase in current with increasing concentration. The I_{pa} *vs.* concentration graph for the Au_{chm}/MWCNT and Au_{grn}/MWCNT electrodes was described by the equations $I_{pa} = 0.0049[MB] + 12.225$ and $I_{pa} = -0.0397[MB] + 17.34$, respectively. Utilizing eqn (26) and (27), the Au_{chm}/MWCNT electrode exhibited a detection limit (LOD) of 20.62 nM and quantification limit (LOQ) of 62.51 nM, while the Au_{grn}/MWCNT electrode exhibited corresponding values of 20.23 nM and 61.30 nM, respectively.

$$\mathrm{LOD} = \frac{3.3 \times \mathrm{SD}}{\mathrm{slope}} \tag{26}$$

$$\mathrm{LOQ} = \frac{10 \times \mathrm{SD}}{\mathrm{Slope}} \tag{27}$$

Scheme 1 shows the reaction mechanism occurring at the surface of both Au_{chm}/MWCNTs and Au_{grn}/MWCNTs. Both electrodes have the same reaction mechanism since the only part of the composite interacting with MB's N^+ is the COO^- part of MWCNTs, while AuNPs based on the synthesis route contributes to the overall properties of the nanocomposite such as conductivity, electrochemical activity, electron transfer, and catalytic activity.

A comparative analysis of the present study with previous studies on detecting MB using various catalysts is summarized in Table 4. Notably, the composite electrodes employed in this study demonstrate higher sensitivity and lower LOD values

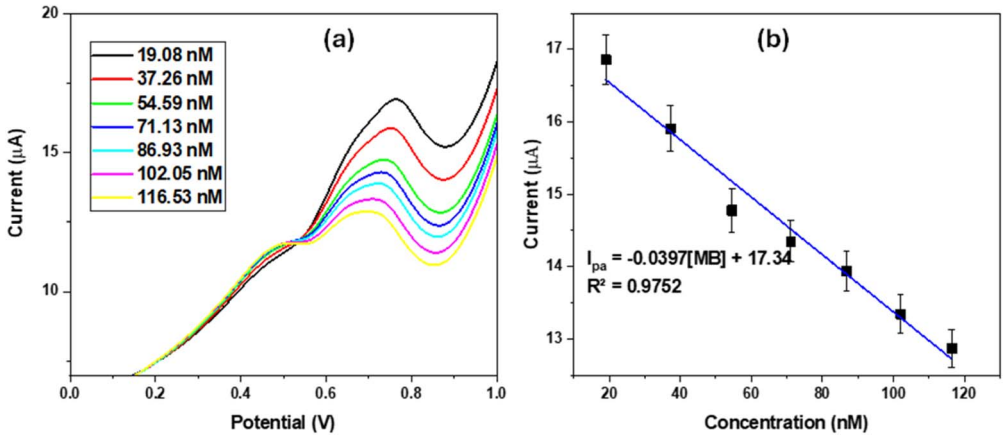

Fig. 15 (a) SWV of Au_{grn}/MWCNTs in MB concentration ranging from 19.08 to 116.53 nm and (b) Au_{chm}/MWCNT linear plot of I_p *vs.* conc.

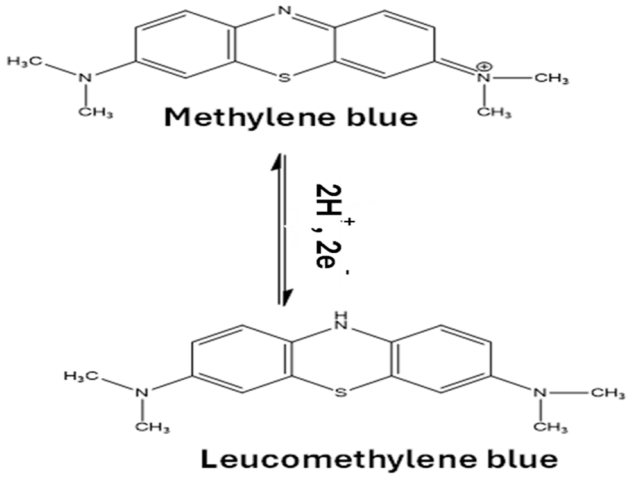

Scheme 1 MB's reaction mechanism at the surface of Au_{chm}/MWCNTs and Au_{grn}/MWCNTs.

compared to some of the previous reports, underscoring the potential of these nanocomposites for electrochemical sensing application.

3.6.7 Interference studies. The development of electrochemical sensors necessitates careful consideration of selectivity, a critical parameter that ensures accurate detection of target analytes in complex matrices amidst potential interferents. This study undertakes an investigation into the selectivity of both green and chemically synthesized Au/MWCNTs towards MB in the presence of sunset yellow dye (SSY), a commonly encountered interferent. Fig. 16(a) and (b) illustrate the detection of MB using Au_{chm}/MWCNT and Au_{grn}/MWCNT nanocomposites, respectively, over a concentration range of 0.9 to 5.10 μM, while maintaining a constant SSY concentration of 0.1 mM. Notably, both nanocomposites exhibited good selectivity.

3.7 Analysis of real-life environmental samples

The sensors' efficacy was investigated using SWV to detect MB in river water. To this end, glassy carbon electrodes modified with Au_{chm}/MWCNTs (GCE-Au_{chm}/MWCNTs) and Au_{grn}/MWCNTs (GCE-Au_{grn}/MWCNTs) nanocomposites were employed. A thorough analysis of the data presented in Tables 5 and 6 revealed that the recovery rates obtained using the GCE-Au_{chm}/MWCNT electrode ranged from 90% to 99%, accompanied by a relative standard deviation (RSD) of 4.78% ($n = 3$).

Table 4 The performance of GCE-Au/MWCNTs in this work compared to the existing literature on MB dye

Electrode	LOD (μm)	Linear range (μm)	Technique	References
NH_2-FMWCNTs	0.00021	0.01–50	SWV	36
MPTMS-Ba	0.475	1.0–14	CV	121
Ibu-AuNPs	0.0039	0.01–1.1	DPV	122
BDD-NWA	0.0072	0.04–10	SWV	123
Co-bhb	0.1	5×10^5 to 35×10^5	CV	124
SD-TNT	0.4	1.0–7.94	CV	125
25FE-19Cr-19Ni-18ti-19mn alloy powder	—	1×10^3 to 5×10^3	CV	126
AuNPs	0.015	0.3–100	DPV	127
CNTs-Auspe	0.1	0.1–10	DPV and SWV	128
GCE-Ag_{chm}/MWCNTs	4.684×10^{-6}	2.927×10^{-6} to 15.652×10^{-6}	SWV	70
GCE-Ag_{grn}/MWCNTs	2.953×10^{-6}	2.927×10^{-6} to 15.652×10^{-6}	SWV	70
GCE-Au_{chm}/MWCNTs	0.02062	0.01908	SWV	This work
GCE-Augrn/MWCNTs	0.02023	0.11633	SWV	This work

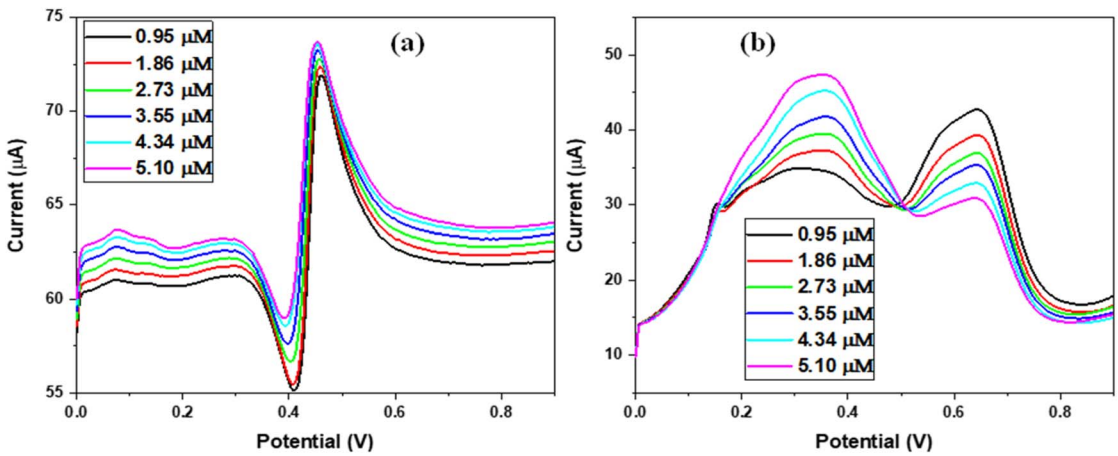

Fig. 16 (a) SWV of Au_{chm}/MWCNTs detecting MB (0.5 V) in the presence of SSY (0.1 and 0.2 V) and (b) Au_{grn}/MWCNTs detecting MB (0.65 V) in the presence of SSY (0.3 V).

Table 5 Recovery of GCE-Au_{chm}/MWCNTs in MB detection in river water

Sample	Added (μM)	Detected (μM)	Recovery (%)	RSD (%)
River water	50	47.2	94	4.78
		49.8	99	
		45.1	90	

Table 6 Recovery of GCE-Au_{grn}/MWCNTs in MB detection in river water

Sample	Added (μM)	Detected (μM)	Recovery (%)	RSD (%)
River water	50	51.1	102	4.90
		52.8	107	
		48.6	97	

Conversely, the GCE-Au_{grn}/MWCNT electrode yielded significantly higher recovery rates, spanning from 97% to 107%. This notable enhancement can be attributed to the sample matrix effect. The water sample's complex matrix, comprising multiple compounds, intensified the analytical signals.[70,129–131] Furthermore, the high recovery percentage observed at GCE-Au_{grn}/MWCNTs was because of an increased surface area and reactivity caused by the green nanocomposite's smaller particle size. The recovery percentages were determined (eqn (18)),[23] highlighting the electrodes' outstanding reliability, sensitivity, and effectiveness in detecting MB in river water samples.

4 Conclusion

This successfully developed and characterised Au/MWCNT nanocomposites synthesized through both chemical and green methods. A rigorous characterization protocol was employed to scrutinize the morphological and spectroscopic attributes of the resultant nanomaterials, leveraging techniques such FTIR, UV-vis, XRD, TEM, and SEM. Furthermore, the electrochemical behaviour of the fabricated electrodes was exhaustively evaluated using CV in both FeCN and MB, revealing that the Au_{grn}/MWCNT electrode exhibited superior electrochemical performance, closely rivaled by the Au_{chm}/MWCNT electrode. EIS also showed two circuits, whereby the material fitted using the double capacitance circuit showed lower R_{ct} values compared to the circuit containing CPE, but the R_{ct} values in FeCN correlated with the CV's oxidation current response of the material in FeCN. The exceptional electrochemical performance of MWCNTs in MB detection can be attributed to their inherent properties, which render them an ideal candidate for MB detection followed by Au_{grn}/MWCNTs, and their response is high because of the synergistic properties of Au_{grn} and MWCNTs combined. The sensitivity of the synthesized nanocomposites was evaluated, yielding LOD and LOQ values of 20.62 nM and 62.51 nM for the Au_{chm}/MWCNT electrode, and 20.23 nM and 61.30 nM for the Au_{grn}/MWCNT electrode, respectively. These results suggest that the Au_{grn}/MWCNT electrode possesses a marginally higher sensitivity due to Au_{grn} showing less agglomeration on SEM and the presence of phytochemical properties from the plant played a significant role in the performance of Au_{grn}/MWCNTs. To assess their practical applicability, the electrodes were tested using the river water sample. The recovery rates achieved by the Au_{chm}/MWCNT electrode ranged from 90% to 99%, while the Au_{grn}/MWCNT electrode demonstrated a recovery rate of 97% to 107%. Overall, the developed nanocomposites showed high sensitivity and dependability for MB detection, highlighting their potential for environmental applications.

Data availability

The data related to the study are included in this article and available upon request.

Author contributions

OEF: conceptualization, supervision, reviewing, and editing. SJM: synthesis and electrochemical investigations, data curation, and interpretation of data. All authors were involved in manuscript writing and reviewing.

Conflicts of interest

The authors declare no conflict of interest.

Acknowledgements

All authors acknowledge NRF-Sasol, MaSIM, and North-West University facilities and support.

References

1 L. Lin, H. Yang and X. Xu, Effects of water pollution on human health and disease heterogeneity: a review, *Front. Environ. Sci.*, 2022, **10**, 880246.
2 K. Bailey, A. Basu and S. Sharma, The environmental impacts of fast fashion on water quality: a systematic review, *Water*, 2022, **14**(7), 1073.
3 K. Gomes, S. Caucci, J. Morris, E. Guenther and J. Miggelbrink, Sustainability transformation in the textile industry—the case of wastewater management, *Bus. Strategy Dev.*, 2024, **7**(1), e324.
4 S. Dardouri and J. Sghaier, Adsorptive removal of methylene blue from aqueous solution using different agricultural wastes as adsorbents, *Korean J. Chem. Eng.*, 2017, **34**(4), 1037–1043.
5 P. R. Ginimuge and S. Jyothi, Methylene blue: revisited, *J. Anaesthesiol., Clin. Pharmacol.*, 2010, **26**(4), 517–520.
6 T. Kofidis, M. Strüber, M. Wilhelmi, M. Anssar, A. Simon, W. Harringer and A. Haverich, Reversal of severe vasoplegia with single-dose methylene blue after heart

transplantation, *J. Thorac. Cardiovasc. Surg.*, 2001, **122**(4), 823–824.

7 P. E. Meissner, G. Mandi, B. Coulibaly, S. Witte, T. Tapsoba, U. Mansmann, J. Rengelshausen, W. Schiek, A. Jahn and I. Walter-Sack, Methylene blue for malaria in Africa: results from a dose-finding study in combination with chloroquine, *Malar. J.*, 2006, **5**, 1–5.

8 E. M. Sloand, C. M. Kessler, C. L. McIntosh and H. G. Klein, Methylene blue for neutralization of heparin, *Thromb. Res.*, 1989, **54**(6), 677–686.

9 A. K. Moorthy, B. G. Rathi, S. P. Shukla, K. Kumar and V. S. Bharti, Acute toxicity of textile dye Methylene blue on growth and metabolism of selected freshwater microalgae, *Environ. Toxicol. Pharmacol.*, 2021, **82**, 103552.

10 I. Pepper, C. P. Gerba and M. L. Brusseau, in *Environmental and Pollution Science*, Elsevier, 2011.

11 A. H. Hashem, E. Saied and M. S. Hasanin, Green and ecofriendly bio-removal of methylene blue dye from aqueous solution using biologically activated banana peel waste, *Sustainable Chem. Pharm.*, 2020, **18**, 100333.

12 P. O. Oladoye, T. O. Ajiboye, E. O. Omotola and O. J. Oyewola, Methylene blue dye: toxicity and potential elimination technology from wastewater, *Results Eng.*, 2022, **16**, 100678.

13 K. Pompapathi, K. S. Anantharaju, P. Karuppasamy, M. Subramaniam, B. Uma, S. Boppanahalli Siddegowda, A. Paul Chowdhury and H. A. Murthy, Visible-light-driven mentha spicata L.-mediated Ag-doped Bi2Zr2O7 nanocomposite for enhanced degradation of organic pollutants, electrochemical sensing, and antibacterial applications, *ACS Environ. Au*, 2024, **4**(2), 106–125.

14 P. Karuppasamy, N. R. N. Nisha, A. Pugazhendhi, S. Kandasamy and S. Pitchaimuthu, An investigation of transition metal doped TiO2 photocatalysts for the enhanced photocatalytic decoloration of methylene blue dye under visible light irradiation, *J. Environ. Chem. Eng.*, 2021, **9**(4), 105254.

15 N. Bélaz-David, L. Decosterd, M. Appenzeller, Y. Ruetsch, R. Chioléro, T. Buclin and J. Biollaz, Spectrophotometric determination of methylene blue in biological fluids after ion-pair extraction and evidence of its adsorption on plastic polymers, *Eur. J. Pharm. Sci.*, 1997, **5**(6), 335–345.

16 H. Borwitzky, W. E. Haefeli and J. Burhenne, Analysis of methylene blue in human urine by capillary electrophoresis, *J. Chromatogr. B*, 2005, **826**(1–2), 244–251.

17 J. Burhenne, K.-D. Riedel, J. Rengelshausen, P. Meissner, O. Müller, G. Mikus, W. E. Haefeli and I. Walter-Sack, Quantification of cationic anti-malaria agent methylene blue in different human biological matrices using cation exchange chromatography coupled to tandem mass spectrometry, *J. Chromatogr. B*, 2008, **863**(2), 273–282.

18 N. F. Gaudette and J. W. Lodge, Determination of methylene blue and leucomethylene blue in male and female Fischer 344 rat urine and B6C3F1 mouse urine, *J. Anal. Toxicol.*, 2005, **29**(1), 28–33.

19 S. B. Turnipseed, J. E. Roybal, S. M. Plakas, A. P. Pfenning, J. A. Hurlbut and A. R. Long, Determination of Methylene Blue in Channel Catfish {Ictalurus punctatus) Tissue by Liquid Chromatography with Visible Detection, *J. AOAC Int.*, 1997, **80**(1), 31–36.

20 S. J. Kim, D. J. Ha and T. S. Koo, Simultaneous quantification of methylene blue and its major metabolite, azure B, in plasma by LC-MS/MS and its application for a pharmacokinetic study, *Biomed. Chromatogr.*, 2014, **28**(4), 518–524.

21 L. Du Plessis, in *The Development of Simple HPLC Methods to Separate Methylene Blue and its Metabolites*, North-West University, 2018.

22 C. Ferrag and K. Kerman, in *Grand Challenges in Nanomaterial-Based Electrochemical Sensors*, Frontiers Media SA, 2020, p. 583822.

23 D. Yang, X. Wang and H. Xu, Enhancing Trace $Pb2^{+}$ Detection via Novel Functional Materials for Improved Electrocatalytic Redox Processes on Electrochemical Sensors: A Short Review, *Catalysts*, 2024, **14**(7), 451.

24 S. Hussain, I. Sadiq, J. Ahmed Baig, F. Sadiq, I. Bux Solangi, K. Akhtar, S. Ahmed Solangi, M. Idress, S. Riaz and S. Naseem, Electrocatalytic sensing of metronidazole by R-type hexagonal nanoferrites modified electrode, *Inorg. Chem. Commun.*, 2023, **153**, 110832.

25 R. Poomporai Vadivel, K. Venkatesh, K. Alagumalai, P. Karuppasamy, X. Arulanandam, M. Ahmad Ansari, B. Amanulla, S. Cheol Kim and S. K. Ramaraj, Fabrication of iron manganese oxide-reduced graphene oxide nanocomposite: A highly effective synergistic electrocatalyst for sensitive metronidazole detection, *Ceram. Int.*, 2024, **50**(21), 44659–44670.

26 M. U. Draz, A. Yaqub, A. T. Jafry, M. Khan and H. Ajab, Electrochemical sensing of B-complex vitamins: current challenges and future prospects with microfluidic integration, *RSC Adv.*, 2024, **14**(15), 10331–10347.

27 S. Kumar, S. Tripathy, A. Jyoti and S. G. Singh, Recent advances in biosensors for diagnosis and detection of sepsis: A comprehensive review, *Biosens. Bioelectron.*, 2019, **124**, 205–215.

28 X. Luo, Advances in nanomaterial-based electrochemical (bio-) sensors, *Microchim. Acta*, 2023, **190**(1), 9.

29 A. Curulli, Nanomaterials in electrochemical sensing area: Applications and challenges in food analysis, *Molecules*, 2020, **25**(23), 5759.

30 J. Baranwal, B. Barse, G. Gatto, G. Broncova and A. Kumar, Electrochemical sensors and their applications: A review, *Chemosensors*, 2022, **10**(9), 363.

31 X. Luo, A. Morrin, A. J. Killard and M. R. Smyth, Application of nanoparticles in electrochemical sensors and biosensors, *Electroanalysis*, 2006, **18**(4), 319–326.

32 C. Kumunda, A. S. Adekunle, B. B. Mamba, N. W. Hlongwa and T. T. Nkambule, Electrochemical detection of environmental pollutants based on graphene derivatives: a review, *Front. Mater. Sci.*, 2021, **7**, 616787.

33 C. Gibi, C.-H. Liu, S. Anandan and J. J. Wu, Recent Advances on Electrochemical Sensors for Detection of Contaminants of Emerging Concern (CECs), *Molecules*, 2023, **28**(23), 7916.

34 C. I. Justino, A. C. Duarte and T. A. Rocha-Santos, Critical overview on the application of sensors and biosensors for clinical analysis, *TrAC, Trends Anal. Chem.*, 2016, **85**, 36–60.
35 N. R. Stradiotto, H. Yamanaka and M. V. B. Zanoni, in *Electrochemical Sensors: A Powerful Tool in Analytical Chemistry*, SciELO Brasil, 2003.
36 M. Hayat, A. Shah, J. Nisar, I. Shah, A. Haleem and M. N. Ashiq, A Novel Electrochemical Sensing Platform for the Sensitive Detection and Degradation Monitoring of Methylene Blue, *Catalysts*, 2022, **12**(3), 306.
37 J. Barek, How to improve the performance of electrochemical sensors via minimization of electrode passivation, *Chemosensors*, 2021, **9**(1), 12.
38 S. J. Malode, M. Ali Alshehri and N. P. Shetti, Nanomaterial-Based Electrochemical Sensors for the Detection of Pharmaceutical Drugs, *Chemosensors*, 2024, **12**(11), 234.
39 D. Wu, J. Zhu, Y. Zheng and L. Fu, Electrochemical Sensing Strategies for Synthetic Orange Dyes, *Molecules*, 2024, **29**(21), 5026.
40 M. Kang, D. Kim, J. Kim, N. Kim and S. Lee, Strategies to Enrich Electrochemical Sensing Data with Analytical Relevance for Machine Learning Applications: A Focused Review, *Sensors*, 2024, **24**(12), 3855.
41 J. I. de Oliveira Filho, M. C. Faleiros, D. C. Ferreira, V. Mani and K. N. Salama, Empowering electrochemical biosensors with air: Overcoming interference for precise dopamine detection in complex samples, *Adv. Intell. Syst.*, 2023, **5**(10), 2300227.
42 A. Karthika, P. Karuppasamy, S. Selvarajan, A. Suganthi and M. Rajarajan, Electrochemical sensing of nicotine using CuWO4 decorated reduced graphene oxide immobilized glassy carbon electrode, *Ultrason. Sonochem.*, 2019, **55**, 196–206.
43 T. M. Oliveira and S. Morais, New generation of electrochemical sensors based on multi-walled carbon nanotubes, *Appl. Sci.*, 2018, **8**(10), 1925.
44 L. Ceroni, S. Benazzato, S. Pressi, L. Calvillo, E. Marotta and E. Menna, Enhanced adsorption of methylene blue dye on functionalized multi-walled carbon nanotubes, *Nanomaterials*, 2024, **14**(6), 522.
45 A. Ghaffar and M. N. Younis, Interaction and thermodynamics of methylene blue adsorption on oxidized multi-walled carbon nanotubes, *Green Process. Synth.*, 2015, **4**(3), 209–217.
46 D. Robati, S. Bagheriyan, M. Rajabi, O. Moradi and A. A. Peyghan, Effect of electrostatic interaction on the methylene blue and methyl orange adsorption by the pristine and functionalized carbon nanotubes, *Phys. E*, 2016, **83**, 1–6.
47 K. Saha, S. S. Agasti, C. Kim, X. Li and V. M. Rotello, Gold nanoparticles in chemical and biological sensing, *Chem. Rev.*, 2012, **112**(5), 2739–2779.
48 G. Nocito, R. Zribi, M. Chelly, L. Pulvirenti, G. Nicotra, C. Bongiorno, A. Arrigo, B. Fazio, G. Neri and F. Nastasi, Photochemical synthesis, characterization, and electrochemical sensing properties of CD–AuNP nanohybrids, *Nanoscale*, 2024, **16**(7), 3571–3582.
49 N. Y. Stozhko, M. A. Bukharinova, E. I. Khamzina and A. V. Tarasov, Electrochemical properties of phytosynthesized gold nanoparticles for electrosensing, *Sensors*, 2021, **22**(1), 311.
50 E. Arslan, E. Biçer, E. Sekmen and S. Çakir, Green synthesis, characterisation of Au and Ag nanoparticles by various bioextracts and their usability at graphite electrode modification, *Turk. J. Chem.*, 2022, **46**(4), 1253–1268.
51 K. K. Bharadwaj, B. Rabha, S. Pati, T. Sarkar, B. K. Choudhury, A. Barman, D. Bhattacharjya, A. Srivastava, D. Baishya and H. A. Edinur, Green synthesis of gold nanoparticles using plant extracts as beneficial prospect for cancer theranostics, *Molecules*, 2021, **26**(21), 6389.
52 Y. Li, T.-Y. Wu, S.-M. Chen, M. A. Ali and F. M. AlHemaid, Green synthesis and electrochemical characterizations of gold nanoparticles using leaf extract of Magnolia kobus, *Int. J. Electrochem. Sci.*, 2012, **7**(12), 12742–12751.
53 P. Saha, M. A. Aziz, M. M. Islam and A. Saleh Ahammad, An Ultra-Sensitive Electrochemical Sensor for Nitrite Based on Green Synthesized Gold Nanoparticles Using Colocasia Esculenta Extract, *ChemNanoMat*, 2024, **10**(11), e202400325.
54 E. G. Döll, E. R. Santana, J. P. Winiarski, L. G. Baumgarten and I. C. Vieira, Green synthesis of gold nanoparticles using peach extract incorporated in graphene for the electrochemical determination of antioxidant butylated hydroxyanisole in food matrices, *Biosensors*, 2023, **13**(12), 1037.
55 C. García-Hernández, C. García-Cabezón, C. Medina-Plaza, F. Martín-Pedrosa, Y. Blanco, J. A. de Saja and M. L. Rodríguez-Méndez, Electrochemical behavior of polypyrrol/AuNP composites deposited by different electrochemical methods: sensing properties towards catechol, *Beilstein J. Nanotechnol.*, 2015, **6**(1), 2052–2061.
56 O. Matvieiev, R. Šelešovská, M. Marton, M. Hatala, R. Metelka, M. Weis and M. Vojs, Effect of different modification by gold nanoparticles on the electrochemical performance of screen-printed sensors with boron-doped diamond electrode, *Sci. Rep.*, 2023, **13**(1), 21525.
57 A. I. Ruiz-Carmuega, C. Garcia-Hernandez, J. Ortiz, C. Garcia-Cabezon, F. Martin-Pedrosa, Á. Sastre-Santos, M. A. Rodríguez-Perez and M. L. Rodriguez-Mendez, Electrochemical sensors modified with combinations of sulfur containing phthalocyanines and capped gold nanoparticles: a study of the influence of the nature of the interaction between sensing materials, *Nanomaterials*, 2019, **9**(11), 1506.
58 J. H. Shim, J. Kim, C. Lee and Y. Lee, Electrocatalytic activity of gold and gold nanoparticles improved by electrochemical pretreatment, *J. Phys. Chem. C*, 2011, **115**(1), 305–309.
59 G. Zhang, Functional gold nanoparticles for sensing applications, *Nanotechnol. Rev.*, 2013, **2**(3), 269–288.
60 Z. Sadiq, S. H. Safiabadi Tali, H. Hajimiri, M. Al-Kassawneh and S. Jahanshahi-Anbuhi, Gold nanoparticles-based colorimetric assays for environmental monitoring and

food safety evaluation, *Crit. Rev. Anal. Chem.*, 2024, **54**(7), 2209–2244.

61 G. Favero, G. Fusco, F. Mazzei, F. Tasca and R. Antiochia, Electrochemical characterization of graphene and MWCNT screen-printed electrodes modified with AuNPs for laccase biosensor development, *Nanomaterials*, 2015, **5**(4), 1995–2006.

62 A. Muhammad, N. A. Yusof, R. Hajian and J. Abdullah, Construction of an electrochemical sensor based on carbon nanotubes/gold nanoparticles for trace determination of amoxicillin in bovine milk, *Sensors*, 2016, **16**(1), 56.

63 S. Rabai, A. Teniou, G. Catanante, M. Benounis, J.-L. Marty and A. Rhouati, Fabrication of AuNPs/MWCNTS/chitosan nanocomposite for the electrochemical aptasensing of cadmium in water, *Sensors*, 2021, **22**(1), 105.

64 Y.-C. Yeh, B. Creran and V. M. Rotello, Gold nanoparticles: preparation, properties, and applications in bionanotechnology, *Nanoscale*, 2012, **4**(6), 1871–1880.

65 S. Kumar, H. Sidhu, A. K. Paul, N. Bhardwaj, N. S. Thakur and A. Deep, Bioengineered multi-walled carbon nanotube (MWCNT) based biosensors and applications thereof, *Sens. Diagn.*, 2023, **2**(6), 1390–1413.

66 S. Mehmood, R. Ciancio, E. Carlino and A. S. Bhatti, Role of Au (NPs) in the enhanced response of Au (NPs)-decorated MWCNT electrochemical biosensor, *Int. J. Nanomed.*, 2018, 2093–2106.

67 L. Wang, Y. Liu and Y. Chen, Effective electrochemical sensor based on Au nanoparticles decorated carboxylated multi-wall carbon nanotube (AuNPS@ c-MWCNTs) nanocomposites for determination of dicapthon pesticide in agricultural food, *Int. J. Electrochem. Sci.*, 2021, **16**(4), 210464.

68 A. D. McFarland, C. L. Haynes, C. A. Mirkin, R. P. Van Duyne and H. A. Godwin, Color my nanoworld, *J. Chem. Educ.*, 2004, **81**(4), 544A.

69 S. Kaviya, J. Santhanalakshmi, B. Viswanathan, J. Muthumary and K. Srinivasan, Biosynthesis of silver nanoparticles using citrus sinensis peel extract and its antibacterial activity, *Spectrochim. Acta, Part A*, 2011, **79**(3), 594–598.

70 S. J. Mokole and O. E. Fayemi, Voltametric detection of methylene blue dye in water at green and chemically synthesized Ag/MWCNT modified electrode, *Mater. Res. Express*, 2024, **11**(10), 105008.

71 S. Gurunathan, J. Han, J. H. Park and J.-H. Kim, A green chemistry approach for synthesizing biocompatible gold nanoparticles, *Nanoscale Res. Lett.*, 2014, **9**, 1–11.

72 A. K. Suresh, D. A. Pelletier, W. Wang, M. L. Broich, J.-W. Moon, B. Gu, D. P. Allison, D. C. Joy, T. J. Phelps and M. J. Doktycz, Biofabrication of discrete spherical gold nanoparticles using the metal-reducing bacterium Shewanella oneidensis, *Acta Biomater.*, 2011, **7**(5), 2148–2152.

73 E. Nivethaa, S. Dhanavel, V. Narayanan, S. N. Kalkura, J. Sivasankari, N. Sivanandham and A. Stephen, CS/Au/MWCNT nanohybrid as an efficient carrier for the sustained release of 5-FU and a study of its cytotoxicity on MCF-7, *RSC Adv.*, 2021, **11**(8), 4584–4592.

74 J. Santos, A. Silva and R. Bretas, Using the carbon nanotube (CNT)/CNT interaction to obtain hybrid conductive nanostructures, *AIP Conf. Proc.*, 2015, 070021.

75 A. Obeid, O. Al-Shuja'a, Y. El-Shekeil, S. Aqeel, M. S. Salit and Z. Al-Washali, New strategy for chemically attachment of Amide group on Multi-walled Carbon Nanotubes surfaces: synthesis, characterization and study of DC electrical conductivity, *Curr. Chem. Lett.*, 2018, 17–26.

76 V. Duc Chinh, G. Speranza, C. Migliaresi, N. Van Chuc, V. Minh Tan and N.-T. Phuong, Synthesis of gold nanoparticles decorated with multiwalled carbon nanotubes (Au-MWCNTs) via cysteaminium chloride functionalization, *Sci. Rep.*, 2019, **9**(1), 5667.

77 R. Tsekov, P. Georgiev, S. Simeonova and K. Balashev, Quantifying the blue shift in the light absorption of small gold nanoparticles, *arXiv*, 2017, preprint, arXiv:1702.04513, DOI: **10.48550/arXiv.1702.04513**.

78 L. Cury, L. Ladeira and A. Righi, Large blue shift in the absorption spectra of BEH-PPV films containing gold nanoparticles, *Synth. Met.*, 2003, **139**(2), 283–286.

79 G. Bajaj and R. Soni, Nanocomposite ZnO/Au formation by pulsed laser irradiation, *Appl. Surf. Sci.*, 2010, **256**(21), 6399–6402.

80 D. Wang, M. J. Hore, X. Ye, C. Zheng, C. B. Murray and R. J. Composto, Gold nanorod length controls dispersion, local ordering, and optical absorption in polymer nanocomposite films, *Soft Matter*, 2014, **10**(19), 3404–3413.

81 R. C. Ferrier Jr, H.-S. Lee, M. J. Hore, M. Caporizzo, D. M. Eckmann and R. J. Composto, Gold nanorod linking to control plasmonic properties in solution and polymer nanocomposites, *Langmuir*, 2014, **30**(7), 1906–1914.

82 S. C. Ray, D. K. Mishra and W.-F. Pong, Optimization of Magnetic Behaviors of Au-NP-Decorated MWCNTs and Reduced Graphene Oxide for Biomedical Applications, *ACS omega*, 2024, **9**(38), 40067–40074.

83 A. Choudhary, T. F. George and G. Li, Conjugation of nanomaterials and nematic liquid crystals for futuristic applications and biosensors, *Biosensors*, 2018, **8**(3), 69.

84 S. Zainab, M. Azeem, S. U. Awan, S. Rizwan, N. Iqbal and J. Rashid, Optimization of bandgap reduction in 2-dimensional GO nanosheets and nanocomposites of GO/iron-oxide for electronic device applications, *Sci. Rep.*, 2023, **13**(1), 6954.

85 J. M. Gisbert-González, W. Cheuquepán, A. Ferre-Vilaplana, E. Herrero and J. M. Feliu, Citrate adsorption on gold: Understanding the shaping mechanism of nanoparticles, *J. Electroanal. Chem.*, 2020, **875**, 114015.

86 M. Y. Marcelino, F. A. Borges, L. Scorzoni, J. de Lacorte Singulani, B. C. Garms, J. C. Niemeyer, N. B. Guerra, G. S. A. P. Brasil, C. U. Mussagy and F. A. de Oliveira Carvalho, Synthesis and characterization of gold nanoparticles and their toxicity in alternative methods to the use of mammals, *J. Environ. Chem. Eng.*, 2021, **9**(6), 106779.

87 M. T. Aljarrah, A. M. Alboull, M. S. Alharahsheh, A. Ashraf and A. Khandakar, Parametric study of gold nanoparticles synthesis under micro-continuous flow conditions, *Molecules*, 2022, **27**(24), 8651.
88 M. Hosny, M. Fawzy, A. M. Abdelfatah, E. E. Fawzy and A. S. Eltaweil, Comparative study on the potentialities of two halophytic species in the green synthesis of gold nanoparticles and their anticancer, antioxidant and catalytic efficiencies, *Adv. Powder Technol.*, 2021, **32**(9), 3220–3233.
89 O. M. El-Borady, M. S. Ayat, M. A. Shabrawy and P. Millet, Green synthesis of gold nanoparticles using Parsley leaves extract and their applications as an alternative catalytic, antioxidant, anticancer, and antibacterial agents, *Adv. Powder Technol.*, 2020, **31**(10), 4390–4400.
90 M. Sivakavinesan, M. Vanaja, R. Lateef, H. A. Alhadlaq, R. Mohan, G. Annadurai and M. Ahamed, Citrus limetta Risso peel mediated green synthesis of gold nanoparticles and its antioxidant and catalytic activity, *J. King Saud Univ., Sci.*, 2022, **34**(7), 102235.
91 S. Mohan, O. S. Oluwafemi, S. P. Songca, D. Rouxel, P. Miska, F. B. Lewu, N. Kalarikkal and S. Thomas, Completely green synthesis of silver nanoparticle decorated MWCNT and its antibacterial and catalytic properties, *Pure Appl. Chem.*, 2016, **88**(1–2), 71–81.
92 Z. Li, L. Fan, T. Zhang and K. Li, Facile synthesis of Ag nanoparticles supported on MWCNTs with favorable stability and their bactericidal properties, *J. Hazard. Mater.*, 2011, **187**(1–3), 466–472.
93 J. Chen, Z. Gao, R. Yang, H. Jiang, L. Bai, A. Shao and H. Wu, New Methylene Blue Covalently Functionalized Graphene Oxide Nanocomposite as Interfacial Material for the Electroanalysis of Hydrogen Peroxide, *Front. Chem.*, 2021, **9**, 788804.
94 S. J. Mokole, A. Aliyu and O. E. Fayemi, Electrochemical detection of dopamine using green and chemical synthesized CuO/PANI nanocomposite modified electrode, *Appl. Phys. A*, 2023, **129**(2), 148.
95 Z. Zhang and Y. Wu, Investigation of the NaBH4-induced aggregation of Au nanoparticles, *Langmuir*, 2010, **26**(12), 9214–9223.
96 K. S. Krishnamurthy Sneha, M. S. Muthuswamy Sathishkumar, K. S. Kim Sok and Y. Y. Yun YeoungSang, Counter ions and temperature incorporated tailoring of biogenic gold nanoparticles, *J. Ovonic Res.*, 2010, 1450–1458.
97 S. Krishnamurthy, A. Esterle, N. C. Sharma and S. V. Sahi, Yucca-derived synthesis of gold nanomaterial and their catalytic potential, *Nanoscale Res. Lett.*, 2014, **9**, 1–9.
98 N. Hamzah, S. Ibrahim and D. H. Tjahjono, Evaluation of phenolic compounds as cross-linkers to improve the qualities of halal gelatin from milkfish scales (Chanos chanos), *Narra J*, 2024, **4**(3), e907.
99 T. V. Ngo, S. Kusumawardani, K. Kunyanee and N. Luangsakul, Polyphenol-modified starches and their applications in the food industry: recent updates and future directions, *Foods*, 2022, **11**(21), 3384.
100 P. Halappa, H. M. Rajashekar and C. Shivakumara, Synthesis and structural characterization of orange red light emitting Sm3+ activated BiOCl phosphor for WLEDs applications, *J. Alloys Compd.*, 2019, **785**, 169–177.
101 A. Maru, H. Kamble, A. Kalarikkal, R. Shah, P. Bhanuse and N. Pradhan, Mg doped ZnO dilute magnetic oxides prepared by chemical method, *Int. J. Chem. Phys. Sci.*, 2020, **5**, 44–49.
102 I. Ahmad, E. Ahmed, M. Ullah, A. Rana, M. Manzoor, M. Rasheed, A. Malik, N. Khalid, M. Ahmad and U. Mehtab, Synthesis and characterization of silver doped zno nanoparticles for hydrogen production, *J. Ovonic Res.*, 2018, **14**(6), 415–427.
103 T. Kalaivani and P. Anilkumar, Synthesis of TiO2: Ce nanoparticles for development of ammonia gas sensors, *J. Mater. Sci.: Mater. Electron.*, 2018, **29**, 100678.
104 L. S. Rao, T. V. Rao, S. Naheed and P. V. Rao, Structural and optical properties of zinc magnesium oxide nanoparticles synthesized by chemical co-precipitation, *Mater. Chem. Phys.*, 2018, **203**, 133–140.
105 A. F. Jaleel and A. S. Wasfi, Gold nanoparticles fabricated by the electrical wire explosion technique, deposited on a porous silicon as an active substrate for surface-enhanced Raman scattering (SERS), *J. Phys.:Conf. Ser.*, 2021, 012094.
106 M. R. Kumalasari, R. Alfanaar and A. S. Andreani, Gold nanoparticles (AuNPs): A versatile material for biosensor application, *Talanta Open*, 2024, **9**, 100327.
107 Y.-H. Won, K. Huh and L. A. Stanciu, Au nanospheres and nanorods for enzyme-free electrochemical biosensor applications, *Biosens. Bioelectron.*, 2011, **26**(11), 4514–4519.
108 R. Segura, J. Pizarro, K. Díaz, A. Placencio, F. Godoy, E. Pino and F. Recio, Development of electrochemical sensors for the determination of selenium using gold nanoparticles modified electrodes, *Sens. Actuators, B*, 2015, **220**, 263–269.
109 D. T, K. Ramachandran, R. Subramani, V. Kanagasabai and M. Anish, Synthesis and Characterisation of Multi Walled Carbon Nanotubes (MWCNTs), *Int. J. Ambient Energy*, 2018, **41**, 1–12.
110 M. Li, M. Luo, J. An and Y. Liu, Choline electrochemical biosensor based on MWCNT-AuNPs and MWCNT-PANI composite nanomaterials, *Microchem. J.*, 2025, **213**, 113609.
111 T. Dodevska and I. Shterev, Nanomaterials as catalysts for the sensitive and selective determination of diclofenac, *ADMET and DMPK*, 2024, **12**(1), 151–165.
112 L. A. Goulart, R. Goncalves, A. A. Correa, E. C. Pereira and L. H. Mascaro, Synergic effect of silver nanoparticles and carbon nanotubes on the simultaneous voltammetric determination of hydroquinone, catechol, bisphenol A and phenol, *Mikrochim. Acta*, 2017, **185**(1), 12.
113 F. A. Adesanya and O. E. Fayemi, Electro-oxidation of pyrene on glassy carbon electrode modified with fMWCNTs/CuO nanocomposite, *Mater. Res. Express*, 2024, **11**(2), 025004.
114 O. E. Fayemi, J. Makgopa and S. E. Elugoke, Comparative electrochemical properties of polyaniline/carbon quantum dots nanocomposites modified screen-printed

carbon and gold electrodes, *Mater. Res. Express*, 2024, **10**(12), 125603.

115 E. Laborda, J. López-Asanza and A. Molina, Theoretical Framework and Guidelines for the Cyclic Voltammetry of Closed Bipolar Cells, *Anal. Chem.*, 2023, **95**(47), 17311–17317.

116 A. Fraczek-Szczypta, E. Menaszek, T. B. Syeda, A. Misra, M. Alavijeh, J. Adu and S. Blazewicz, Effect of MWCNT surface and chemical modification on in vitro cellular response, *J. Nanopart. Res.*, 2012, **14**, 1–14.

117 S. Mohan, O. S. Oluwafemi, S. P. Songca, D. Rouxel, P. Miska, F. B. Lewu, N. Kalarikkal and S. Thomas, Completely green synthesis of silver nanoparticle decorated MWCNT and its antibacterial and catalytic properties, *Pure Appl. Chem.*, 2016, **88**(1–2), 71–81.

118 T. S. Munonde and P. N. Nomngongo, Nanocomposites for electrochemical sensors and their applications on the detection of trace metals in environmental water samples, *Sensors*, 2020, **21**(1), 131.

119 Z. Wu, S. Yang and W. Wu, Shape control of inorganic nanoparticles from solution, *Nanoscale*, 2016, **8**(3), 1237–1259.

120 G. Maduraiveeran and W. Jin, Nanomaterials based electrochemical sensor and biosensor platforms for environmental applications, *Trends Environ. Anal. Chem.*, 2017, **13**, 10–23.

121 I. K. Tonlé, E. Ngameni, H. L. Tcheumi, V. Tchiéda, C. Carteret and A. Walcarius, Sorption of methylene blue on an organoclay bearing thiol groups and application to electrochemical sensing of the dye, *Talanta*, 2008, **74**(4), 489–497.

122 S. S. Hassan, A. Nafady, Sirajuddin, A. R. Solangi, M. S. Kalhoro, M. I. Abro and S. T. H. Sherazi, Ultra-trace level electrochemical sensor for methylene blue dye based on nafion stabilized ibuprofen derived gold nanoparticles, *Sens. Actuators, B*, 2015, **208**, 320–326.

123 S. He, K. Lin, S. Cheng, N. Gao, J. Liu and H. Li, Improving Trace Detection of Methylene Blue by Designing Nanowire Array on Boron-Doped Diamond as Electrochemical Electrode, *Coatings*, 2024, **14**(6), 762.

124 S. Sangeetha, G. Krishnamurthy and M. S. Raghavan, Electrochemical sensing and photocatalytic degradation of methylene blue (MB) dye by cobalt-beta hydroxy benzoate complex, *Mater. Sci. Semicond. Process.*, 2019, **101**, 164–173.

125 P. Soto, C. Salamanca-Neto, J. Moraes, E. Sartori, G. G. Bessegato, F. Lopes and L. Almeida, A novel sensing platform based on self-doped TiO2 nanotubes for methylene blue dye electrochemical monitoring during its electro-Fenton degradation, *J. Solid State Electrochem.*, 2020, **24**(8), 1951–1959.

126 S. Rajendrachari, V. M. Adimule, G. K. Jayaprakash and A. Pandith, Electrochemical oxidation of methylene blue dye in wastewater using mechanically alloyed high entropy alloy modified carbon paste electrode using cyclic voltammetry, *Mater. Res. Express*, 2023, **10**(5), 054003.

127 M. Lin, H. Han and D. Pan, Voltammetric determination of total dissolved iron in coastal waters using a glassy carbon electrode modified with reduced graphene oxide, Methylene Blue and gold nanoparticles, *Microchim. Acta*, 2015, **182**, 805–813.

128 R. García-González, A. Costa-García and M. T. Fernández-Abedul, Enhanced detection of the potential electroactive label methylene blue by electrode nanostructuration with carbon nanotubes, *Sens. Actuators, B*, 2014, **202**, 129–136.

129 A. L. Squissato, E. M. Richter and R. A. Munoz, Voltammetric determination of copper and tert-butylhydroquinone in biodiesel: A rapid quality control protocol, *Talanta*, 2019, **201**, 433–440.

130 R. S. Nunes and É. T. Cavalheiro, Caffeine determination at a carbon fiber ultramicroelectrodes by fast-scan cyclic voltammetry, *J. Braz. Chem. Soc.*, 2012, **23**, 670–677.

131 M. N. Catrinck, L. L. Okumura, A. A. Silva, A. A. Saczk and M. F. Oliveira, New and sensitive electroquantification of sulfentrazone in soil by differential-pulse voltammetry, *J. Braz. Chem. Soc.*, 2015, **26**(9), 1751–1759.